



HAL
open science

Finite element and experimental structural analysis of endodontic rotary file made of Cu-based single crystal SMA considering a micromechanical behavior model

Paul Xolin, Christophe Collard, Marc Engels-Deutsch, Tarak Ben Zineb

► To cite this version:

Paul Xolin, Christophe Collard, Marc Engels-Deutsch, Tarak Ben Zineb. Finite element and experimental structural analysis of endodontic rotary file made of Cu-based single crystal SMA considering a micromechanical behavior model. *International Journal of Solids and Structures*, 2021, 221, pp.180-196. 10.1016/j.ijsolstr.2021.01.015 . hal-03228880

HAL Id: hal-03228880

<https://hal.univ-lorraine.fr/hal-03228880>

Submitted on 9 May 2023

HAL is a multi-disciplinary open access archive for the deposit and dissemination of scientific research documents, whether they are published or not. The documents may come from teaching and research institutions in France or abroad, or from public or private research centers.

L'archive ouverte pluridisciplinaire **HAL**, est destinée au dépôt et à la diffusion de documents scientifiques de niveau recherche, publiés ou non, émanant des établissements d'enseignement et de recherche français ou étrangers, des laboratoires publics ou privés.



Distributed under a Creative Commons Attribution - NonCommercial 4.0 International License

Finite element and experimental structural analysis of endodontic rotary file made of Cu-based single crystal SMA considering a micromechanical behavior model

Paul Xolin^a, Christophe Collard^b, Marc Engels-Deutsch^{a,c}, Tarak Ben Zineb^a

^aUniversité de Lorraine, CNRS, Arts et Métiers ParisTech, LEM3, F-54000 Nancy, France

^bCNRS, CEMES, UPR 8011, F-31400 Toulouse, France

^cUniversité de Lorraine, Faculté d'Odontologie de Lorraine, F-54000 Nancy, France

Abstract

Shape Memory Alloys (SMAs) are widely used in endodontics as instruments for root canal preparation namely endodontic rotary files. Despite their high performances, compared to stainless steel instruments, it is still possible to enhance their cutting efficiency by acting on their shape and material properties. As an example, increasing the exhibited reversible martensitic transformation strain makes them more flexible without decreasing their mechanical strength. It becomes possible with single crystal SMAs. Cu-based (Cu-Al-Be, Cu-Zn-Al, Cu-Al-Mn) single crystal SMAs start emerging and can reach about 12% of martensitic transformation strain, in addition to their interesting antimicrobial properties. This study investigates, both numerically and experimentally, the development of endodontic files made of Cu-based single crystal SMAs. The numerical analysis is carried out by the finite element method. The geometry of the instrument is parameterized. Depending on the applied boundary conditions, bending, torsion, or combined bending-torsion loadings are represented. A micromechanical constitutive law is implemented in Abaqus via the UMAT subroutine to describe the thermomechanical behavior of the Cu-based single crystal SMA. Following the thus obtained numerical results, Coltene-Micromega company has manufactured endodontic file prototypes made of Cu-Al-Be sin-

Email address: tarak.ben-zineb@univ-lorraine.fr (Tarak Ben Zineb)

Preprint submitted to International Journal of Solids and Structures December 12, 2020

gle crystal SMA. A specific setup applying the same boundary conditions of torsion-bending loading, is used to characterize these SMA file prototypes. The good agreement between experimental and numerical responses, for a combined bending-torsion loading, proves the relevance of the proposed approach and the pertinence of considering Cu-based SMAs for endodontic file applications.

Keywords: Shape Memory Alloy, Endodontic files, Cu-based single crystal SMA, Finite element analysis, experimental analysis, combined bending-torsion

1 1. Introduction

2 Root canal treatment is a dental procedure used to treat inflamed or/and
3 infected tooth pulp. It enables a patient to retain a tooth in a healthy state on
4 his dental arcade. The procedure is often complicated and, once the diagnosis is
5 made, consists in isolating the tooth, opening the crown, shaping and cleaning
6 the root canal, and finally filling it with a biocompatible sealer. To remove the
7 dental pulp and its organo-mineral content, endodontic files are needed. The
8 root canal preparation in endodontics relies on manual then rotary file capac-
9 ity to remove organic content, microorganisms and predentin and to follow the
10 curved areas while operating without causing any damage and any instrument
11 failure. This capacity was mainly improved during the last decades. Manual
12 stainless steel files were replaced by rotary ones with the same material making
13 the root canal preparation more efficient and with fewer cases of failure. How-
14 ever, stainless steel rotary files had difficulties to follow the relatively curved
15 and conical shape of the root canal for a given tooth. This curvature could have
16 a circular arc shape or a plane/tridimensional “S” shape. This is due to their
17 very weak exhibited reversible deformation induced by elasticity only. That is
18 why endodontic rotary files made of NiTi SMAs emerged naturally as an inter-
19 esting alternative to stainless steel ones ([Pedrinha et al., 2018](#)). In fact, SMAs
20 and in particular NiTi alloys are able to deliver much higher reversible defor-
21 mation thanks to the reversible martensitic transformation strain. It enables

22 the more flexible rotary file to better follow simple or double curved root canals
23 during the preparation process. These properties allow the use of mechanized
24 files driven in a rotation motion from generally 150 rpm to 350-600 rpm (Zelada
25 et al., 2002; Padavala and Ganapathy, 2019). In addition, NiTi SMAs are also
26 bio-compatible and show a good resistance to corrosion, a high strength stress
27 and a high resistance to fatigue under bending and torsion loading (Shen et al.,
28 2011; Jamleh et al., 2019). They have two main specific thermomechanical
29 behaviors governed by forward and reverse martensitic phase transformation:
30 superelasticity effect (SE) and shape memory effect (SME), with respectively
31 a self recovering and a thermally assisted recovering of the martensitic trans-
32 formation strain after unloading. The major available rotary endodontic files
33 are SE even if SME ones, with more flexibility induced by martensite detwin-
34 ning at quasi-constant buccal temperature, start to emerge and are known in
35 endodontics as heat treated rotary files (Prados-Privado et al., 2019). However,
36 continuously rotating NiTi files operate with the inherent risk associated with
37 torque and cyclic fatigue failures. To decrease this risk, files were used in a
38 mechanical reciprocating movement, turning a specific distance clockwise, then
39 rotating counterclockwise (Karatas et al., 2016). Over the past years, a huge
40 number of carried out research and development works enabled to enhance the
41 cutting performances of these rotary files (Schaefer and Oitzinger, 2008). They
42 acted on optimization of material parameters related to (SE) and (SME) mech-
43 anisms, (Zinelis et al., 2007), on geometrical parameters as cross section shape,
44 tip diameter, taper, pitch, operative length (Ahamed et al., 2018; Ha et al., 2017;
45 De Arruda Santos et al., 2014; Arbab Chirani et al., 2011; Chevalier et al., 2018),
46 and also on control parameters as speed rotation for continuous and reciprocating
47 motion and maximum torsion torque. It has been determined that the tip
48 diameter, the taper, and the cross section properties (shape, area and inertia),
49 have in addition to SMA properties, an influence on the bending and torsion
50 flexibilities (or stiffnesses) and on the torsion and fatigue resistance (Schäfer and
51 Tepel, 1999; Rodrigues et al., 2016; Chi et al., 2017). The fatigue behavior of
52 these NiTi SMA endodontic files and the corresponding induced fracture modes

53 were also investigated by (Ferreira et al., 2017; Aidasani et al., 2017) leading to
54 the same conclusions. (Kim et al., 2012; McGuigan et al., 2013; Martins et al.,
55 2017) showed that fracture while operating is induced by bending or torsion or
56 both combined loading. Therefore, considering these results, rotating endodon-
57 tic files performances were highly improved making more efficient, reproducible
58 and safer the canal root preparation and reducing its duration. However, these
59 improvements mainly focus on NiTi rotary files. Recently our research group
60 showed that it is possible to even more improve performances of rotary files
61 by considering Cu-based single crystal SMAs (Cu-SC-SMA) as for example the
62 Cu-Al-Be alloy (Vincent et al., 2015, 2017). Using this SMA family should also
63 contribute to the reduction of the root canal preparation time thanks to the
64 antimicrobial properties of copper (Vincent et al., 2018). Copper is a powerful
65 antimicrobial agent. Microorganisms survive only a few minutes on copper sur-
66 faces (Grass et al., 2011; Prado et al., 2012) especially at 37°C and in conditions
67 of 100% relative humidity (buccal conditions) (Ojeil et al., 2013). Associated
68 with hydrogen peroxide, an endodontic irrigant, copper is able to kill bacte-
69 ria in a very short time through the release of hydroxyl radicals (Hartemann
70 et al., 1995). Conversely, sodium hypochlorite, the most widely used irrigation
71 solution in endodontics, requires 60 minutes of contact time to eliminate mi-
72 croorganisms (Spratt et al., 2001). Contrary to NiTi single crystals, it is easier
73 to manufacture Cu-SC-SMA wires that are well adapted to process rotary files.
74 Moreover, they have very interesting properties: (i) antimicrobial effect during
75 root canal preparation and (ii) much higher flexibility induced by martensitic
76 transformation strain that can go up to 12%. In addition, it is worth noting that
77 polycrystal Cu-based SMAs present very high incompatibilities between grains
78 inducing high internal stresses and fracture below low reversible transformation
79 strains (about 3 or 4%) which also justifies the choice of Cu-SC-SMA.
80 However, it has been shown that such Cu-SC-SMA wires, with a [1 0 0] crys-
81 tallographic orientation in the axis direction, exhibit a very low transformation
82 strain (low volume fraction of martensite) under torsion loading leading to an
83 effective behavior close to the elastic one which is highly anisotropic. Therefore,

84 for given geometrical parameters, the obtained global response of the rotary en-
85 dodontic instrument under torsion loading is stiffer than under bending loading
86 (Sittner et al., 2003). Indeed, when the instrument rotation is hampered by
87 the machined dentin, torsional loading occurs inducing the instrument failure.
88 A part from it will then remain inside the root canal making it very difficult
89 to eliminate. (Vincent et al., 2015) studied by the finite element method the
90 influence of geometrical parameters on responses of Cu-SC-SMA rotary files sub-
91 jected to bending and torsion loading following the Standard ISO-3630-1 (Int.
92 Org. for Standardization, 2008). This study considers a macroscopic thermo-
93 mechanical constitutive model proposed by (Peultier et al., 2006) and improved
94 by (Chemisky et al., 2011). For this preliminary study, the adopted behavior
95 model cannot accurately predict the specific torsional response of Cu-SC-SMA.
96 In fact, the experimental analysis of the martensitic transformation process for
97 these alloys, when subjected to torsion loading, shows an activation of very
98 few martensite variants with a very low corresponding volume fraction (Tokuda
99 et al., 1995; Bouvet et al., 2003; Casciati et al., 2007). It is related to the high
100 incompatibility between martensite variants favorably oriented with respect to
101 the torsion loading direction. It manifests through the moment-rotation global
102 response with a high slope close to the elastic shear modulus and a very weak
103 hysteresis size. Micromechanical models with crystalline plasticity-like formula-
104 tion overcome such drawbacks of phenomenological behavior models. They de-
105 scribe the thermomechanical behavior at the grain scale (each grain is assumed
106 as a single crystal) by considering all potentially active variants of martensite.
107 Each variant is characterized by a set of habit plane-twinning direction, and a
108 volume fraction. Berveiller-Patoor’s research group proposed a micromechani-
109 cal constitutive law based on this approach (Patoor et al., 1996). They derived
110 a macroscopic model more adapted to polycrystalline Cu-based SMAs by ap-
111 plying a self consistent scale transition technique to a Representative Volume
112 Element (RVE) composed of a high number of grains. Each grain has a different
113 crystallographic orientation related to the measured texture (Entemeyer et al.,
114 2000). Other models considering the same approach are also available in liter-

115 ature and detailed in the review paper (Cissé et al., 2016). The single crystal
116 version, initially proposed by (Patoor et al., 1996), improved by (Niclaeys et al.,
117 2002; Merzouki et al., 2010; Collard and Ben Zineb, 2012) is implemented in
118 the finite element code Abaqus. It well describes the martensite variant acti-
119 vation in a Cu-based single crystal SMA, particularly for torsion loading. It is
120 then more adapted to predict the torsional response of Cu-SC-SMA rotary files.
121 Therefore, the present paper details the numerical analysis of rotary prototype
122 made of Cu-SC-SMA considering the aforementioned micromechanical constitu-
123 tive model. It is subjected to respectively bending, torsion and bending-torsion
124 loading. The combined bending-torsion loading occurs on the instrument when
125 it becomes difficult to shape the dentin; in that case, the instrument cannot
126 freely rotate which adds the torsion sollicitation to the bending. The geometry
127 of this rotary file is inspired from already used NiTi files and described with
128 a CAD model developed with Catia[®] and exported to Abaqus[®]. It is meshed
129 with a tetrahedral continuum solid element with quadratic interpolation. The
130 applied boundary conditions and loading respect the recommendation of the
131 ISO Standard 3630-1, (Int. Org. for Standardization, 2008). The identification
132 of the material parameters and the qualification of obtained numerical results
133 rely on experimental results carried out using a specific setup (Xolin et al.,
134 2020). It allows to apply bending and torsion loading in combined or separated
135 ways. Prototypes are processed by Coltene-Micromega[®] using Cu-SC-SMA
136 wires manufactured by Nimesis[®]. The obtained numerical results correctly cor-
137 relate with experimental results and prove the following original features: (i)
138 finite element analysis considering micromechanical constitutive law predicts
139 in a more accurate way the response in torsion of rotary files made of Cu-SC-
140 SMA, (ii) combining bending with torsion for these rotary files reduces their
141 torsional stiffness and then moderates the aforementioned torsional response
142 weakness, (iii) considering the interesting antimicrobial properties of Cu and
143 despite this torsional response weakness, it should be possible to develop new
144 and innovative versions of rotary files made of Cu-SC-SMA. In fact, it shows
145 that responses of Cu-SC-SMA rotary endodontic files are close to the ones of

146 commercial instruments made of NiTi. This is true for both separated and com-
147 bined bending-torsion loadings. Indeed, obtained values of rotations and their
148 induced moments are in the same range as what is measured for commercial
149 instruments. Furthermore, the analysis of sensitivity to geometrical parameters
150 also leads to the same tendencies for commercial instruments (Gavini et al.,
151 2018).

152 The present paper is organized as follows: after the introduction, section 2
153 details the finite element numerical model with geometry, meshing, boundary
154 conditions, loading cases and the adopted micromechanical constitutive model
155 and its implementation in the finite element code Abaqus[®]. Section 3 presents
156 the experimental testing device and the Cu-SC-SMA prototypes. Differential
157 Scanning Calorimetry (DSC), tensile, bending, torsion and combined bending-
158 torsion tests are performed to identify the material parameters of the microme-
159 chanical constitutive model describing the Cu-SC-SMA thermomechanical be-
160 havior. Bending, torsion and combined bending-torsion loadings are applied to
161 validate the proposed model. Section 4 presents the adopted Taguchi design of
162 experiment (DOE) in order to determine the influence of geometrical parame-
163 ters on the equivalent response in combined bending-torsion loading. Section
164 5 presents an overall discussion of the obtained results. The last section gives
165 some conclusions and prospects.

166 **2. Finite element response analysis of the rotary endodontic file** 167 **made of Cu-SC-SMA**

168 *2.1. Introduction*

169 The proposed finite element analysis aims at predicting the global response
170 of the proposed rotary endodontic file made of Cu-SC-SMA and to analyze the
171 corresponding local state, at each material point, in terms of stresses, strains,
172 activated martensite variants and their corresponding volume fractions. The
173 adopted geometrical model is parameterized allowing to analyze the sensitiv-
174 ity of the rotary file response to the geometrical parameters. Applied boundary

175 conditions are consistent with the ISO Standard 3630-1 ([Int. Org. for Standard-](#)
 176 [ization, 2008](#)). They induce a bending-torsion loading applied in combined or
 177 separated ways. The geometry is meshed with tetrahedral continuum elements
 178 and a mesh refinement convergence is carried out. A micromechanical consti-
 179 tutive model describes the thermomechanical behavior of the Cu-based single
 180 crystal SMA. This finite element analysis allows to predict the effect of the tor-
 181 sion on the global bending-torsion response of the studied rotary endodontic
 182 files.

183 2.2. Geometry, mesh, boundary conditions and loading

184 The studied Cu-SC-SMA endodontic file presents a parameterized geometry
 185 defined by figure 1. It presents a cylindrical part characterized by its diameter
 186 and a tapered helical part characterized by its cross-section shape, its length,
 187 its taper, its constant or variable pitch and its tip diameter. The variation
 188 of these geometrical parameters allows to analyze their effects on the global
 189 bending-torsion response. For each set of geometrical parameters, the CAD
 190 software CATIA[®] generates the corresponding instrument geometry which is
 exported into the finite element code Abaqus[®]. Then the meshing process

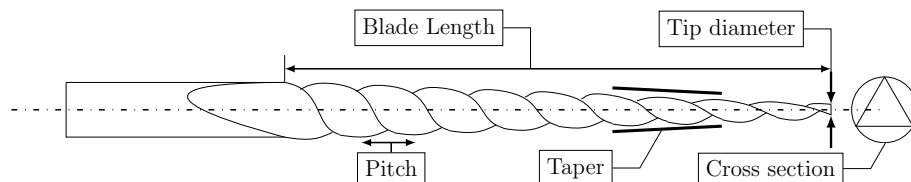


Figure 1: Parametrized geometry of a studied rotary endodontic file.

191
 192 is applied. It considers tetrahedral continuum elements with 10 nodes using
 193 quadratic interpolation (labeled in Abaqus[®] C3D10) and a given number of
 194 intervals of variable size in each edge. This size takes into account the evolution
 195 of the stress state and a predicted area of the martensitic transformation under
 196 bending-torsion loading. Figure 2 presents an example of the obtained mesh for
 197 the helical part after taking into account the assigned geometrical values and
 198 the convergence of the refinement mesh process. It leads to a model with 21 500

elements. Regarding the boundary conditions, a part of the instrument with

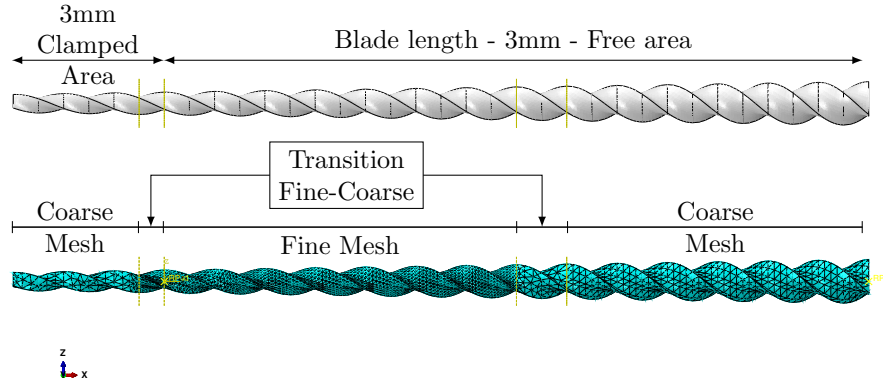


Figure 2: Example of obtained mesh for the helical part of the instrument.

199

200 a 3 mm length starting from its tip is clamped. Two rotations corresponding
 201 to bending and torsion are applied in two reference points as depicted in figure
 202 3. This leads to three loading cases: torsion, bending and combined torsion-
 203 bending. As the instrument is generally rotating with a constant speed, the
 204 analysis assumes a quasi-static loading. Also note that the boundary conditions
 205 can be applied to any wire or prototype instrument with different cross-section
 206 shape, diameter, taper and pitch length.

207 *2.3. Micromechanical constitutive law for Cu-SC-SMA and its implementation*
 208 *in a finite element code*

209 The thermomechanical behavior of the Cu-SC-SMA is described by a con-
 210 stitutive model, developed by (Patoor et al., 1996), and (Niclaeys et al., 2002).
 211 Its implementation in Abaqus via the subroutine UMAT, initially undertaken
 212 by (Merzouki et al., 2010; Collard and Ben Zineb, 2012), is deeply redrafted in
 213 this work leading to an updated version enhancing the convergence process and
 214 reducing computation CPU time. It is based on a crystalline plasticity-like ap-
 215 proach and describes the activation of martensite variants in the crystalline
 216 lattice and its effect on the macroscopic thermomechanical behavior. This

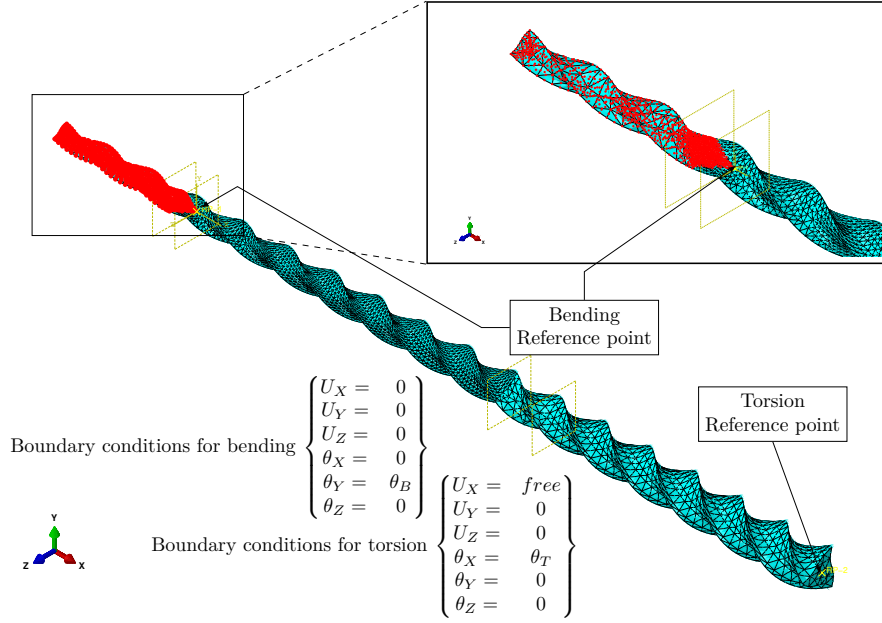


Figure 3: Applied boundary conditions for bending and torsion.

217 model presents 24 scalar internal variables corresponding to volume fractions
 218 of martensite variants. Each variant is defined with a set of two vectors. One
 219 is normal to the given habit plane, \vec{n} , whereas the other defines the twinning
 220 direction, \vec{m} , table 1 and figure 4. They are expressed in the local coordinate
 221 system of the single crystal. A rotation matrix defines the orientation of the
 222 local coordinate system, related to the single crystal, with respect to the global
 223 coordinate system. It characterizes the single crystal lattice orientation. The
 224 intrinsic transformation strain $\tilde{\varepsilon}_{ij}^n$ for any martensite variant (n) depends on
 225 their two vectors \vec{n}^n and \vec{m}^n and a constant transformation amplitude g as
 226 follows:

$$\tilde{\varepsilon}_{ij}^n = \frac{1}{2}g(m_i^n n_j^n + m_j^n n_i^n) = \frac{1}{2}gR_{ij}^n \quad (1)$$

227 where R^n is the symmetric part of the Schmid tensor for the variant (n). In the
 228 case of multi-variants simultaneously active, the global transformation strain
 229 is the resultant of all active variant transformation strains weighted by their

Table 1: Values of \vec{n} and \vec{m} for Cu-Al-Be single crystal SMA .

Variant	n_1	n_2	n_3	m_1	m_2	m_3
1	-0.168	0.688	0.705	-0.121	-0.725	0.678
2	-0.168	0.705	0.688	-0.121	0.678	-0.725
3	0.168	0.688	0.705	0.121	-0.725	0.678
4	0.168	0.705	0.688	0.121	0.678	-0.725
5	-0.688	-0.168	0.705	0.725	-0.121	0.678
6	-0.705	-0.168	0.688	-0.678	-0.121	-0.725
7	-0.688	0.168	0.705	0.725	0.121	0.678
8	-0.705	0.168	0.688	-0.678	0.121	-0.725
9	-0.168	-0.688	0.705	-0.121	0.725	0.678
10	-0.168	-0.705	0.688	-0.121	-0.678	-0.725
11	0.168	-0.688	0.705	0.121	0.725	0.678
12	0.168	-0.705	0.688	0.121	-0.678	-0.725
13	0.705	-0.168	0.688	0.678	-0.121	-0.725
14	0.688	-0.168	0.705	-0.725	-0.121	0.678
15	0.705	0.168	0.688	0.678	0.121	-0.725
16	0.688	0.168	0.705	-0.725	0.121	0.678
17	0.688	-0.705	0.168	-0.725	-0.678	0.121
18	0.705	-0.688	0.168	0.678	0.725	0.121
19	-0.688	0.705	0.168	0.725	0.678	0.121
20	-0.705	0.688	0.168	-0.678	-0.725	0.121
21	-0.705	-0.688	0.168	-0.678	0.725	0.121
22	-0.688	-0.705	0.168	0.725	-0.678	0.121
23	0.705	0.688	0.168	0.678	-0.725	0.121
24	0.688	0.705	0.168	-0.725	0.678	0.121

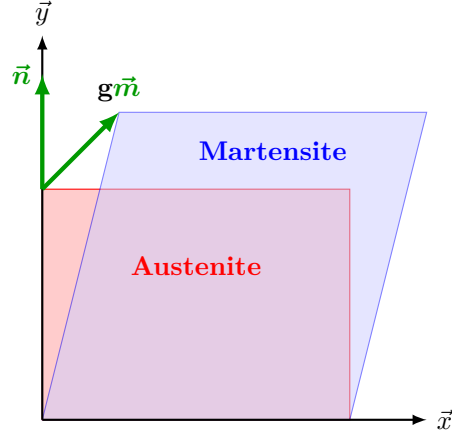


Figure 4: Definition of Habit plane and twinning direction where \vec{n} , \vec{m} and g are the normal of the habit plane, the twinning direction and the transformation displacement respectively.

230 respective volume fractions ($f^n = \frac{V_n}{V_{RVE}}$) as follows:

$$\varepsilon_{ij}^{tr} = \sum_n \tilde{\varepsilon}_{ij}^n f^n \quad (2)$$

231 where V_n is the volume occupied by the variant n and V_{RVE} is the total volume
 232 of the Representative Volume Element (RVE) characterizing a given material
 233 point. The phase transformation process is then characterized by the volume
 234 fraction of the 24 variants assumed as internal variables. These volume fractions
 235 are constrained by martensitic transformation saturation leading to $0 \leq f^n \leq 1$
 236 and $\sum_n f^n \leq 1$. By considering the defined global transformation strain in
 237 addition to the classical elastic and thermal expansion strains, and applying
 238 the first principle of thermodynamics, the micromechanical constitutive model
 239 derives from the following assumed expression of the Gibbs free energy expressed
 240 at the lattice scale:

$$\Delta G(\boldsymbol{\sigma}, T, f^n) = \sigma_{ij} \varepsilon_{ij} - W_{elas} - \Delta G_{ch} - W_{inter} \quad (3)$$

241 where $\boldsymbol{\sigma}$, $\boldsymbol{\varepsilon}$ and T are respectively the stress and strain tensors and the tem-
 242 perature, in a material point, and where W_{elas} , ΔG_{ch} , W_{inter} are respectively
 243 the elastic energy, the chemical energy variation between the austenitic and

244 martensitic phases and the interface energy. This interface energy is assumed
 245 negligible due to the flat shape of martensite variants. After some intermedi-
 246 ate developments detailed in (Siredey et al., 1999), the final expression of the
 247 Gibbs free energy is depicted by equation (4), where α , δ_{ij} , T_0 , T_I and B are
 248 the thermal expansion coefficient, the Kröneckers symbol, the thermodynamic
 249 temperature equilibrium between austenitic and martensitic phases, the initial
 250 temperature of the material and the chemical energy respectively.

$$\begin{aligned} \Delta G(\boldsymbol{\sigma}, T, f^n) = & \frac{1}{2} \sigma_{ij} \mathbb{S}_{ijkl} \sigma_{kl} + \sigma_{ij} \varepsilon_{ij}^{tr} + \alpha \delta_{ij} (T - T_I) \sigma_{ij} \\ & + B(T - T_0) \sum_n f^n - \frac{1}{2} \sum_{n,m} f^n H^{nm} f^m \end{aligned} \quad (4)$$

251 The total energy $\boldsymbol{\sigma} : \boldsymbol{\varepsilon}$ is split into an elastic part, a transformation part related
 252 to the transformation strain $\boldsymbol{\varepsilon}^{tr}$ and a thermal expansion part related to the
 253 expansion tensor. The expansion tensor is assumed isotropic and controlled by
 254 the scalar α . The elastic energy is expressed as a function of the stress tensor
 255 and the fourth order elasticity tensor \mathbb{S} . The chemical energy linearly depends
 256 on the temperature variation and volume fraction of variants. The last term in
 257 equation (4) represents the interaction energy related to internal stresses. It is
 258 induced by incompatibilities between martensite variants. In order to simplify
 259 equations, the interaction between each variant is represented in a matrix H^{nm}
 260 given in table 2. It lists the compatibilities and incompatibilities between all
 261 variants. Taking into account the constraints on the volume fraction of each
 262 variant modifies the expression of Gibbs energy and adds the following terms :

$$\psi_{const} = \sum_n \lambda_1^n f^n + \lambda (1 - \sum_n f^n) \quad (5)$$

It leads to the following expression of the Lagrangian:

$$\begin{aligned} \mathcal{L} = & \sigma_{ij} \varepsilon_{ij} - \Delta G_{ch} - W_{elas} - W_{inter} - \psi_{const} \\ = & \frac{1}{2} \sigma_{ij} \mathbb{S}_{ijkl} \sigma_{kl} + \sigma_{ij} \varepsilon_{ij}^{tr} + \alpha \delta_{ij} (T - T_I) \sigma_{ij} - B(T - T_0) \sum_n f^n \\ & - \frac{1}{2} \sum_{n,m} f^n H^{nm} f^m - (\sum_n \lambda_1^n f^n + \lambda (1 - \sum_n f^n)) \end{aligned} \quad (6)$$

Table 2: Interaction matrix describing compatibilities (C) and incompatibilities (I) between variants.

	1	2	3	4	5	6	7	8	9	10	11	12	13	14	15	16	17	18	19	20	21	22	23	24
1	C	C	C	C	I	I	C	I	C	I	C	I	I	C	I	I	I	I	I	C	C	I	I	I
2	C	C	C	C	I	I	I	C	I	C	I	C	C	I	I	I	I	I	C	I	I	C	I	I
3	C	C	C	C	C	I	I	I	C	I	C	I	I	I	I	C	I	C	I	I	I	I	C	I
4	C	C	C	C	I	C	I	I	I	C	I	C	I	I	C	I	C	I	I	I	I	I	I	C
5					C	C	C	C	C	I	I	I	I	C	I	C	C	I	I	I	I	C	I	I
6					C	C	C	C	I	C	I	I	C	I	C	I	I	C	I	I	C	I	I	I
7					C	C	C	C	I	I	C	I	I	C	I	C	I	I	C	I	I	I	I	C
8					C	C	C	C	I	I	I	C	C	I	C	I	I	I	I	C	I	I	C	I
9									C	C	C	C	I	I	I	C	I	I	I	C	C	I	I	I
10									C	C	C	C	I	I	C	I	I	I	C	I	I	C	I	I
11									C	C	C	C	I	C	I	I	I	C	I	I	I	I	C	I
12									C	C	C	C	C	I	I	I	C	I	I	I	I	I	I	C
13													C	C	C	C	I	C	I	I	C	I	I	I
14													C	C	C	C	C	I	I	I	I	C	I	I
15													C	C	C	C	I	I	I	C	I	I	C	I
16													C	C	C	C	I	I	C	I	I	I	I	C
17																	C	C	C	C	I	C	I	C
18																	C	C	C	C	C	I	C	I
19																	C	C	C	C	I	C	I	C
20																	C	C	C	C	C	I	C	I
21																					C	C	C	C
22																					C	C	C	C
23																					C	C	C	C
24																					C	C	C	C

263 where λ_1^n and λ are Lagrangian multipliers allowing to ensure the transforma-
 264 tion saturation conditions. The application of the Clausius-Duhem condition
 265 integrating the expression of the Lagrangian \mathcal{L} leads to the decomposition of
 266 strains and expressions of driving forces for martensite variants:

$$\left(\underbrace{\left(\left(\frac{\partial \mathcal{L}}{\partial \boldsymbol{\sigma}} - \boldsymbol{\varepsilon} \right) : \dot{\boldsymbol{\sigma}} + \frac{\partial \mathcal{L}}{\partial T} \dot{T} + \sum_n \left(\frac{\partial \mathcal{L}}{\partial f^n} \dot{f}^n + \frac{\partial \mathcal{L}}{\partial \lambda_1^n} \dot{\lambda}_1^n \right) + \frac{\partial \mathcal{L}}{\partial \lambda} \dot{\lambda} \right)}_{\dot{\mathcal{L}}} \right) \geq 0 \quad (7)$$

$$\left(-S^{RVE} \dot{T} - \vec{q} \cdot \frac{\vec{grad} T}{T} \right)$$

267 where S^{RVE} is the entropy of the RVE, \vec{q} is the heat flux induced by dissipation
 268 and T the current temperature of the RVE. Dot over symbols represent their
 269 rate form. Equation (7) leads to the following equations:

$$\begin{cases} \mathbb{S}_{ijkl} \sigma_{kl} + \alpha \delta_{ij} (T - T_I) + \varepsilon_{ij}^{tr} - \varepsilon_{ij} = 0 \\ -B \sum_n f^n - S^{RVE} = 0 \\ g \sigma_{ij} R_{ij}^n - B(T - T_0) e^n - \sum_m H^{nm} f^m - \lambda_1^n + \lambda e^n = F_{yield}^n \end{cases} \quad (8)$$

270 where (e^1, \dots, e^k) is a basis of \mathbb{R}^k defined as $e_i^n = \begin{cases} 0 & \text{if } i \neq n \\ 1 & \text{if } i = n \end{cases}$.

271 The two first driving forces are equal to zero because they correspond to ther-
 272 moelasticity occurring without dissipation whereas the third driving force is
 273 related to phase transformation occurring with dissipation. This justifies the
 274 introduction of a yield force F_{yield}^n associated to each active variant (n) taking
 275 a different value during forward and reverse transformation. The temperature
 276 gradient term becomes equal to zero by assuming a uniform temperature in the
 277 whole RVE. Combining equations (8) and their rate form allows to determine
 278 the rate of volume fraction of martensite \dot{f}^n for each active variant (n) which
 279 reads:

$$\dot{f}^n = \sum_m \hat{H}_{nm}^{-1} \left[\tilde{\varepsilon}_{ij}^m \mathbb{C}_{ijkl} \dot{\varepsilon}_{kl} - \left(\tilde{\varepsilon}_{pq}^m \mathbb{C}_{pqrs} \alpha_{rs} + B e^m \right) \dot{T} \right] \quad (9)$$

280 where the fourth order tensor $\mathbb{C} = \mathbb{S}^{-1}$ is the elasticity tensor and $\hat{H}_{nm} =$
 281 $\left(H^{nm} + \tilde{\varepsilon}_{ij}^n \mathbb{C}_{ijkl} \tilde{\varepsilon}_{kl}^m \right)$ is a $k^v \times k^v$ reversible matrix where k^v is the number of

282 active variants. Combining the rate form of equations (8) and (9) allows to de-
 283 rive the rate form of the micromechanical based thermomechanical constitutive
 284 equations for the Cu-Al-Be single crystal SMA that reads:

$$\dot{\sigma}_{ij} = l_{ijkl}\dot{\epsilon}_{kl} - m_{ij}\dot{T} \quad (10)$$

$$\text{where } \begin{cases} l_{ijkl} = \mathbb{C}_{ijkl} - \sum_{n,m} \mathbb{C}_{ijrs} \tilde{\epsilon}_{rs}^n \hat{H}_{nm}^{-1} \tilde{\epsilon}_{pq}^m \mathbb{C}_{pqkl} \\ m_{ij} = \mathbb{C}_{ijkl} \alpha \delta_{kl} - \sum_{n,m} \mathbb{C}_{ijrs} \tilde{\epsilon}_{rs}^n \hat{H}_{nm}^{-1} (B e^m + \tilde{\epsilon}_{pq}^m \mathbb{C}_{pqkl} \alpha \delta_{kl}) \end{cases}$$

285 These constitutive equations are solved with an iterative method based on the
 286 return mapping approach. The obtained numerical tool is implemented in
 287 Abaqus[®] via the subroutine UMAT. The numerical resolution is detailed in
 288 (Collard and Ben Zineb, 2012). The implementation process in Abaqus via
 289 the subroutine UMAT is initially carried out in (Merzouki et al., 2010). It is
 290 redrafted in a deep way in this work enabling to enhance the convergence pro-
 291 cess and to reduce the computation CPU time. This behavior model presents
 292 metallurgical parameters as transformation temperatures and crystallographic
 293 characteristics as lattice orientation and habit plane and transformation direc-
 294 tion for all variants. It also needs to identify phenomenological parameters as
 295 the elastic coefficients, the compatibility and incompatibility coefficients, the
 296 transformation amplitude g and the yield forces for each variant n , F_{yield}^n . Re-
 297 sults issued from this finite element analysis are compared to the ones obtained
 298 experimentally. The experimental protocol is detailed in the next section.

299 **3. Experimental response analysis of the rotary endodontic file made** 300 **of Cu-SC-SMA**

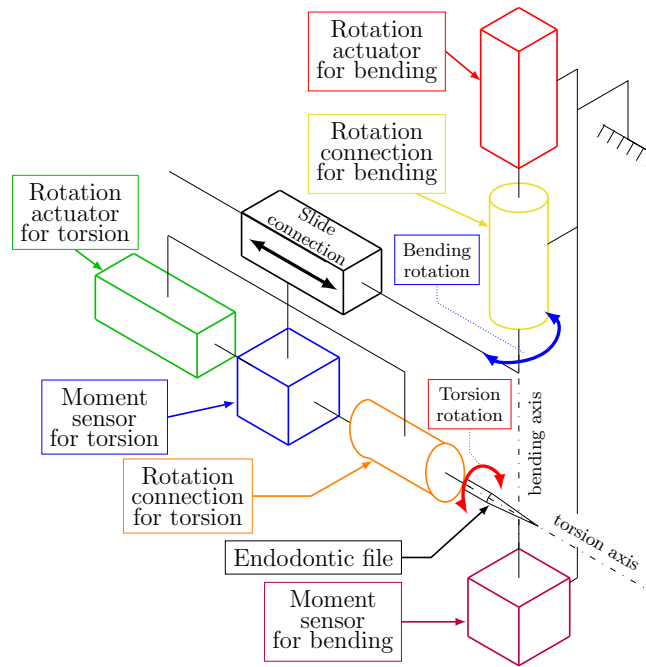
301 The experimental part of this study has a double objective: (i) the identifi-
 302 cation of material parameters and (ii) the validation of the FE based numerical
 303 approach developed in the previous section. In this section, the testing device for
 304 combined bending torsion loadings is briefly presented, then the experimental
 305 protocol is detailed.

306 *3.1. Experimental setup for combined bending-torsion loading*

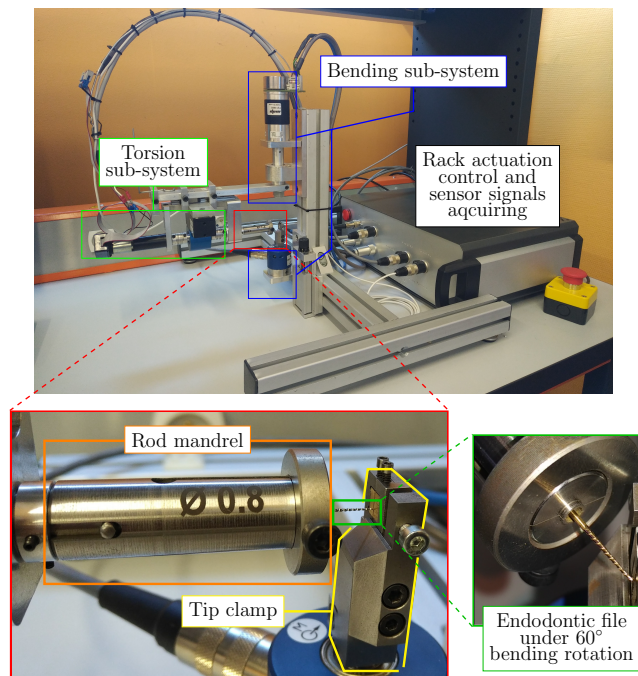
307 The experimental testing device is designed to study the bending and torsion
308 responses of endodontic files under bending, torsion or combined bending-torsion
309 loadings. It is based on the standard ISO 3630-1 ([Int. Org. for Standardiza-](#)
310 [tion, 2008](#)). The main goal of these tests on endodontic file is to determine
311 its flexibility and its resistance to torsional and bending loadings. Indeed, a
312 bending loading is applied on the endodontic file when it has to follow the path
313 of a curved root canal, and a torsion loading is applied due to the continuous
314 rotation movement which allows the file to progress inside the narrow root canal
315 and shape it. However, both bending and torsion loadings applied on the en-
316 dodontic file are combined during the endodontic treatment and represent the
317 most severe loading case. The considered testing device is able to measure the
318 bending, torsion and combined bending-torsion loadings. It is composed as two
319 subsystems: (i) a subsystem for torsion and (ii) a subsystem for bending. The
320 kinematic principle and a detailed picture of the testing device are depicted by
321 figures [5a](#) and [5b](#) respectively. The endodontic file is clamped 3 mm from its
322 tip end and on its rod end 17 mm from the tip. It is loaded in torsion and
323 bending by two rotation actuators. The first rotation is applied around the
324 endodontic file axis whereas the second is applied around an axis perpendicular
325 to this latter. Two corresponding sensors are associated to these actuators in
326 order to measure induced moments. This testing device allows to apply an up
327 to 60° rotation amplitude with 30 N.mm measured torque in bending and 20
328 N.mm torque with no limitation rotation in torsion. Figure [6](#) shows the possible
329 applied loading paths of bending or torsion (figure [6a](#)) and combined bending-
330 torsion (figure [6b](#)). ([Xolin et al., 2020](#)) gives more details about this testing
331 device.

332 *3.2. Material parameter identification with Cu-SC-SMA wire*

333 Uniaxial tests at room temperature and DSC tests are carried out to iden-
334 tify Cu-SC-SMA material parameters for the micromechanical behavior model
335 ([Merzouki et al., 2010](#); [Collard and Ben Zineb, 2012](#)). Then, Cu-SC-SMA wires

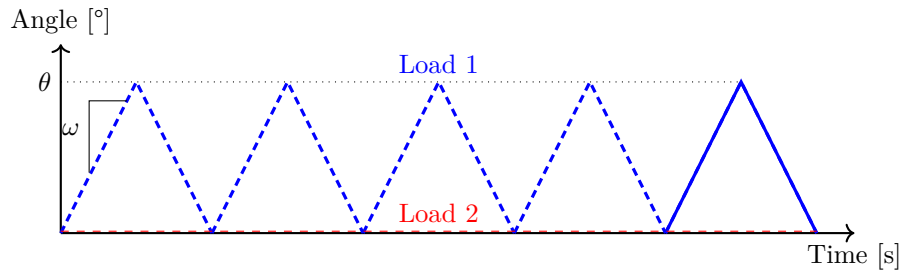


(a) Principle scheme of the testing device

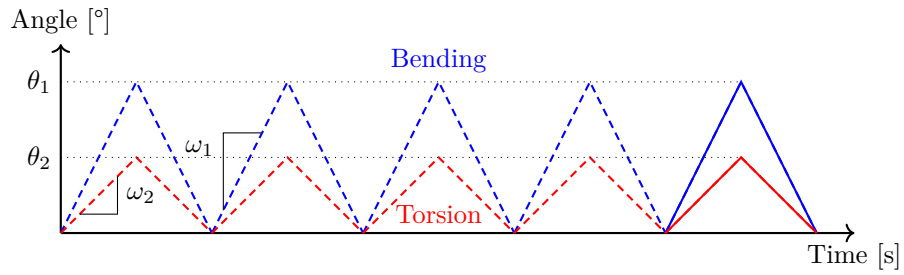


(b) Detailed picture of the testing device

Figure 5: Presentation of the testing device.



(a) Loading path for simple bending or torsion. Load 1 is equated with bending with an angle θ of 60° and a rotation speed ω of $3^\circ.s^{-1}$ for a simple load of bending. It is equated with torsion with an angle θ of 30° and a rotation speed ω of $1.5^\circ.s^{-1}$ for a simple load of torsion. Load 2 is the complementary load, set as 0° .



(b) Loading path for combined bending-torsion. Bending load is applied with an angle θ_1 of 60° and a rotation speed ω_1 of $3^\circ.s^{-1}$. Torsion load is applied with an angle θ_2 of 30° and a rotation speed ω_2 of $1.5^\circ.s^{-1}$.

Figure 6: Schematic description of the applied loads on endodontic files.

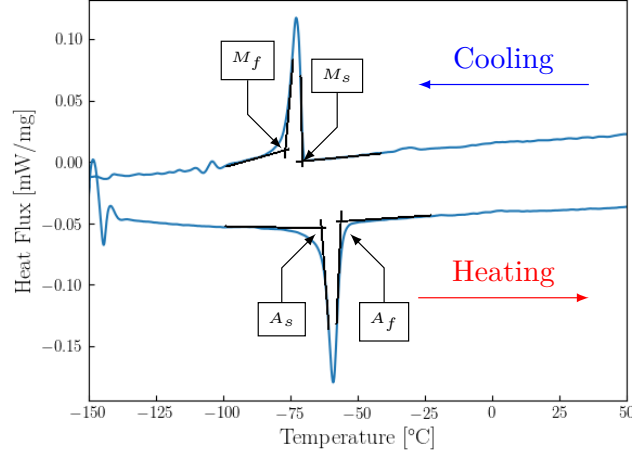


Figure 7: DSC results for a Cu-SC-SMA wire between +50°C and -150°C.

336 are experimentally and numerically tested in bending, torsion and combined
 337 bending-torsion. The numerical responses issued from the micromechanical
 338 model are compared to the experimental ones in order to check the ability
 339 for the model to correctly predict wire tension response.

340 Figure 7 shows results of DSC tests on Cu-SC-SMA wire. They consist in
 341 heating the sample up to 50°C then in cooling it down to -150°C twice and
 342 in measuring the heat flux. The obtained results show two peaks, one while
 343 cooling and one while heating, which are characteristic of forward and reverse
 344 martensitic transformation respectively. The cooling peak is located between
 345 -70°C and -78°C which determines M_s and M_f , the start and finish tempera-
 346 tures for direct martensitic transformation, respectively. The heating peak is
 347 visible between -63°C and -57°C which determines A_s and A_f , the start and
 348 finish temperatures for reverse martensitic transformation, respectively. Figure
 349 8 shows the uniaxial tension test for a Cu-SC-SMA wire of 0.79 mm diameter
 350 subjected to 10 cycles of 8.5% strain. In addition, experimental tests of 30°
 351 of bending, 5° of torsion and respectively 30° and 6° of combined bending and
 352 torsion are realized on Cu-SC-SMA wires. Applied loadings are selected to show

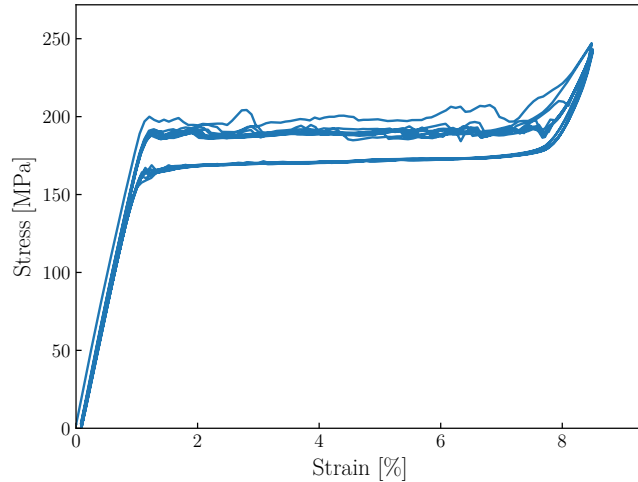


Figure 8: Uniaxial tension response of Cu-SC-SMA wire of 0.79 mm submitted to 10 cycles of 8.5% strain.

353 high deformation responses and not overpass range measurement of sensor. Fig-
 354 ure 9 shows responses of these tests. Figure 9a gives the bending moment of a
 355 Cu-SC-SMA wire subjected to bending and combined bending-torsion loading.
 356 The elastic domain in both cases is similar until the activation of martensitic
 357 transformation. Stiffness during transformation is more important in the case
 358 of pure bending. Regarding the torsion moment of wire subjected to torsion
 359 and combined bending-torsion loadings (figure 9b), responses to both loadings
 360 show a high stiffness. Torsion loading on wire shows a linear response with very
 361 low transformation. But, when torsion is combined with bending, the marten-
 362 sitic transformation occurs in wire since the response of the material exhibits
 363 a non linear behavior and a hysteresis between loading and unloading path.
 364 Also, it is notable that the elastic domain of responses in pure and combined
 365 bending-torsion has different stiffnesses.

366 In the following, the micromechanical model is used to represent the behavior
 367 of Cu-SC-wire under tension, bending, torsion and combined bending-torsion
 368 loadings.

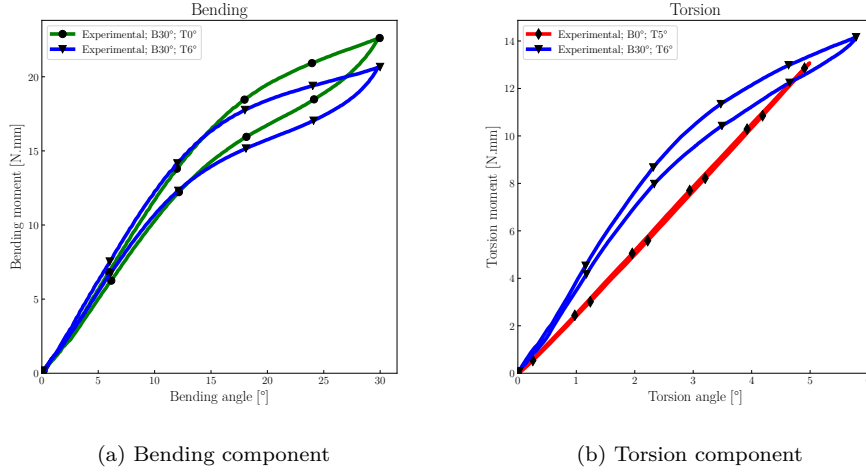


Figure 9: Cu-SC-SMA wire response under bending, torsion and combined bending-torsion loadings.

369 *3.3. Numerical and experimental comparison and material parameters identi-*
 370 *fication*

371 DSC tests, uniaxial tensile test, tests of bending, torsion and combined
 372 bending-torsion are used to identify material parameters. DSC tests are used
 373 to determine temperatures M_s , M_f , A_s and A_f . Elastic coefficients C_{11} , C_{12}
 374 and C_{44} for austenite and martensite are identified from uniaxial tensile tests.
 375 These tests also provide the maximum strain transformation.

376 According to the symmetric cubic elasticity approach (Belkahl, 1990), ma-
 377 terial parameters presented in table 3 are used to identify the material param-
 378 eters the micromechanical constitutive law describing the behavior of Cu-SC-SMA.
 379 Figure 10 compares the 10th cycle of uniaxial tension of figure 8 with the nu-
 380 merical response of a unique cubic element submitted to 8.5% strain.

381 To complete material parameters identification, bending, torsion and com-
 382 bined bending-torsion simulations are numerically predicted with previously
 383 identified parameter. Numerical simulations are conducted with the boundary
 384 conditions presented in section 2.2 to represent experimental loadings. Cu-SC-SMA

C_{11}^A [MPa]	C_{12}^A [MPa]	C_{44}^A [MPa]	A_f [°C]
123192	94200	110838	-57
C_{11}^M [MPa]	C_{12}^M [MPa]	C_{44}^M [MPa]	M_s [°C]
93456	94200	84084	-70
α [°C ⁻¹]	B [MPa °C ⁻¹]	C [MPa]	I [MPa]
1.5e-5	0.14	20-250	2500
g	ϕ_1 [°]	Φ [°]	ϕ_2 [°]
0.139	2	0	0

Table 3: Material parameters of Cu-SC-SMA wire used with micromechanical model

385 wires are represented with 27900 tetrahedron elements with quadratic interpo-
386 lation (codification: C3D10) in Abaqus[®] software. Figure 11 shows the compar-
387 ison between experimental and numerical results for these loadings.

388 3.4. Comparison between numerical and experimental responses of Cu-SC-SMA 389 endodontic file prototypes

390 Endodontic file prototypes are manufactured from Cu-SC-SMA wire. They
391 are tested under combined bending torsion loading with the testing device de-
392 scribed in section 3.1. In addition, the numerical finite element model previously
393 presented is used with a geometrical modeling of the blade of the endodontic
394 file prototype. Both experimental and numerical responses are compared to es-
395 timate the capacity of the model to represent a complex Cu-SC-SMA structure
396 of endodontic file prototypes. The numerical model provides additional infor-
397 mation compared to experiments such as stress state and martensitic variant
398 volume fractions into the Cu-SC-SMA. Figure 12 shows the manufactured tested
399 prototypes (figure 12a) and the corresponding finite element model (figure 12b).
400 They have a two-edged cross section and their geometrical parameters are pre-
401 sented in table 4. The finite element model is composed of 41600 tetrahedron
402 elements with quadratic interpolation and represents only the blade of the pro-
403 totype to reduce computing time. Three prototypes are tested in bending, torsion

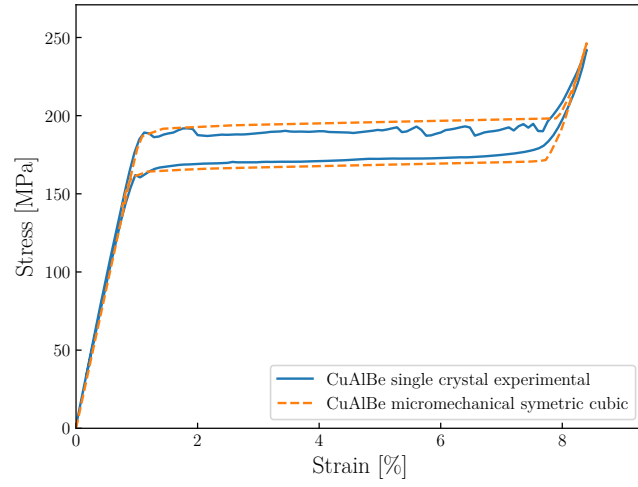


Figure 10: Experimental and numerical comparison of uniaxial tensile response of Cu-SC-SMA wire of 0.79 mm.

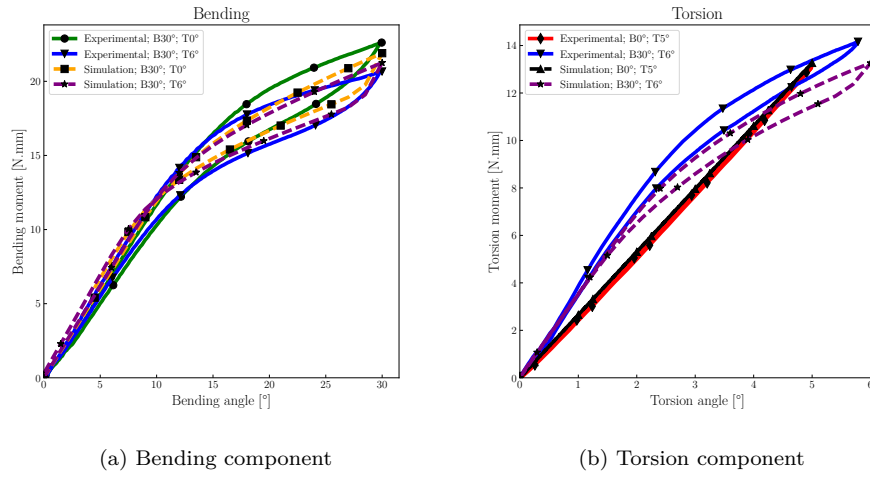
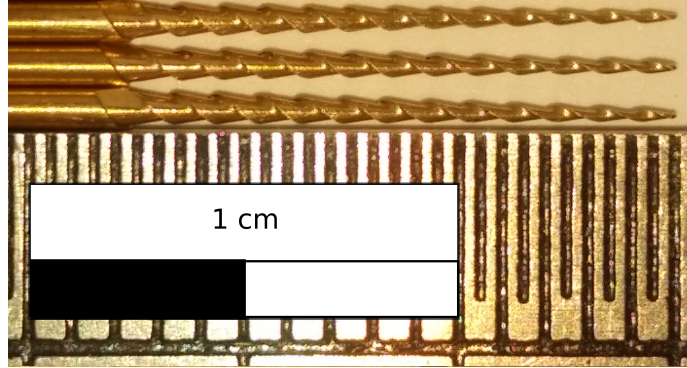
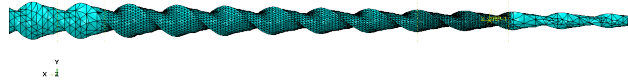


Figure 11: Experimental and numerical comparison of Cu-SC-SMA wire response under bending, torsion and combined bending-torsion loadings.



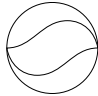
(a) Cu-SC-SMA endodontic file prototypes



(b) Modeled finite element of Cu-SC-SMA endodontic file prototypes

Figure 12: Single crystal endodontic file prototypes.

Table 4: Geometrical parameters of the tested prototypes.

Cross-section	Tip diameter	Taper	Pitch
	0.28 mm	4 %	1 mm

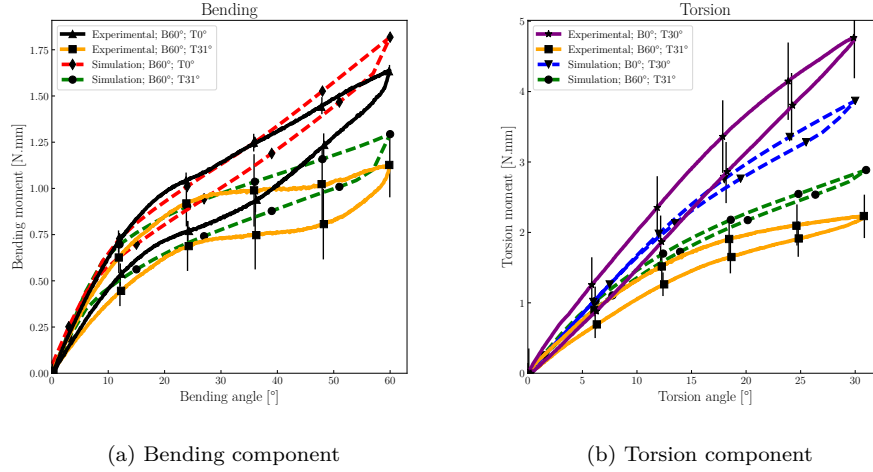


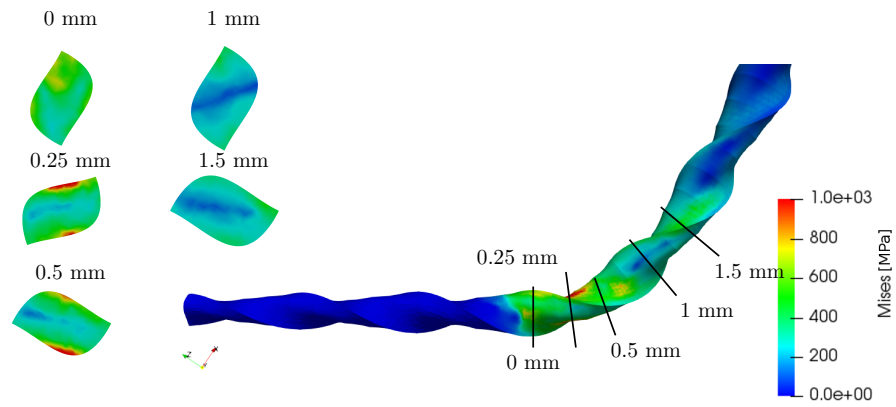
Figure 13: Compararion between experimental and numerical responses under bending, torsion and combined bending-torsion loadings of Cu-SC-SMA endodontic file prototypes with a tip diameter of 0.28 mm, 4% taper and two edges cross section.

404 and combined bending-torsion loadings. Their responses are averaged and the
 405 standard deviation is displayed. The applied bending and torsion rotations are
 406 respectively equal to 60° and 30°. Figure 13 presents experimental averaged
 407 responses of prototypes under bending, torsion and combined bending-torsion
 408 loadings. It is associated with numerical responses obtained with the finite
 409 element model of equivalent geometrical endodontic file prototypes. It shows
 410 that the numerical model predicts with a fairly good correlation the experimen-
 411 tal response of the instrument. The effect of bending-torsion combination is
 412 retranscribed by the model but some differences still exist. Martensitic trans-
 413 formation starts earlier for the numerical model and the stiffness in torsion is
 414 underestimated.

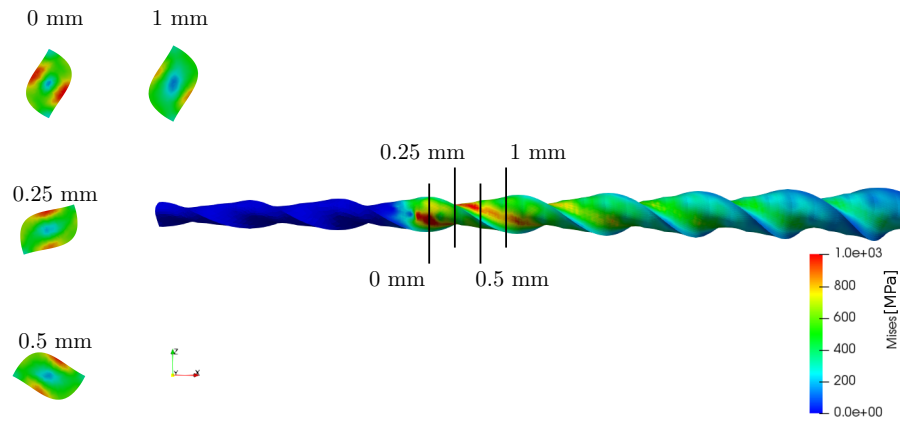
415 3.5. Stress and martensite volume fraction distributions

416 The presented finite element model allows to predict the local stress and
 417 martenistic volume fraction in any material point of the instrument. Figures 14
 418 and 15 depict the numerically obtained response for an endodontic file prototype

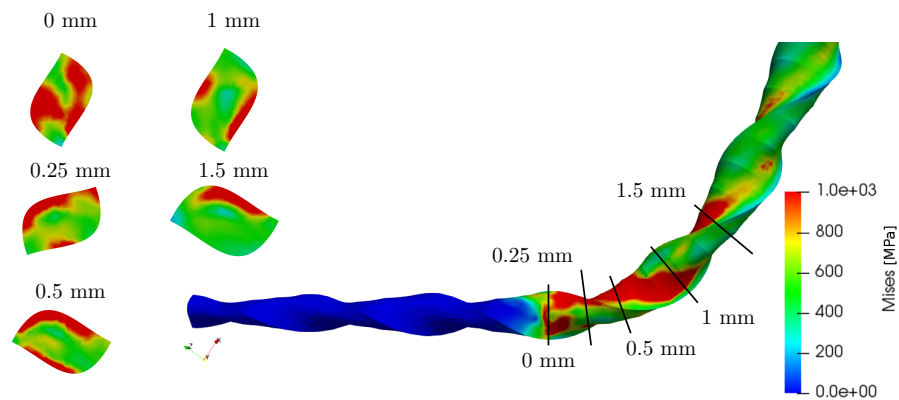
419 with a tip diameter of 0.28 mm, a 4% taper and a two-edged cross section, un-
420 der bending, torsion and combined bending-torsion loadings. Bending loading
421 induces a local stress concentration (figure 14a) in a zone close to the clamped
422 area. Figure 15a shows that martensite appears in this zone subjected to ten-
423 sion and compression. Figure 14b shows the results of torsion loading. A high
424 stress state appears in all blade structures. It corresponds to a high stiffness of
425 numerical and experimental responses. The stress distribution is mainly con-
426 centrated in the center of the blade faces, close to the clamped area. Moreover,
427 the numerical model predicts a low value of volume fraction of martensite (fig-
428 ure 15b) for the Cu-SC-SMA endodontic file prototype in torsion. For combined
429 bending-torsion loading (figure 14c), high stress levels concentrate in the bended
430 zone of the instrument. The stress distribution is induced by a superposition
431 of the stresses obtained by bending and by torsion with the addition of the
432 complex geometry effect. Figure 15c shows the volume fraction of martensite
433 for the combined bending-torsion loadings. It follows the stress distribution,
434 visible for the 0 mm, 0.25 mm, 0.5 mm cuts. However, 1 mm and 1.5 mm cuts
435 show differences in the distribution of stress and volume fraction of martensite.
436 For the 1 mm cut, on figure 15c, volume fraction of martensite is concentrated
437 in inner and outer part of the bended area when the stress distribution (figure
438 14c) corresponds to torsion loading. Moreover, the numerical model allows to
439 determine the activated martensite variants and their associated volume frac-
440 tion in each material point. Figure 16 gives, for the main active variants, the
441 zone where each variant occurs with its associated volume fraction. These vari-
442 ants are 7, 13, 14 and 22 defined in table 1. Their distributions show that each
443 martensite variant occurs separately and partially cohabits with other variants
444 depending on their compatibilities (table 2). Variant 14 occurs in the inner side
445 of the bended area (subjected to a compression stress) next to variants 7 and
446 22. According to table 2, variants 7-22 are incompatible, but 7-14 and 14-22 are
447 compatible. Variant 13 occurs especially in the outer side of the bended area.
448 Moreover, variants in tension and compression areas are different. Variants 13



(a) Bending

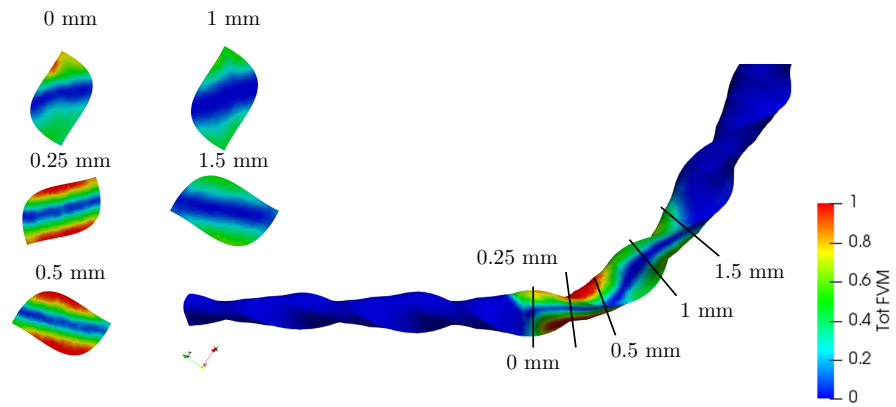


(b) Torsion

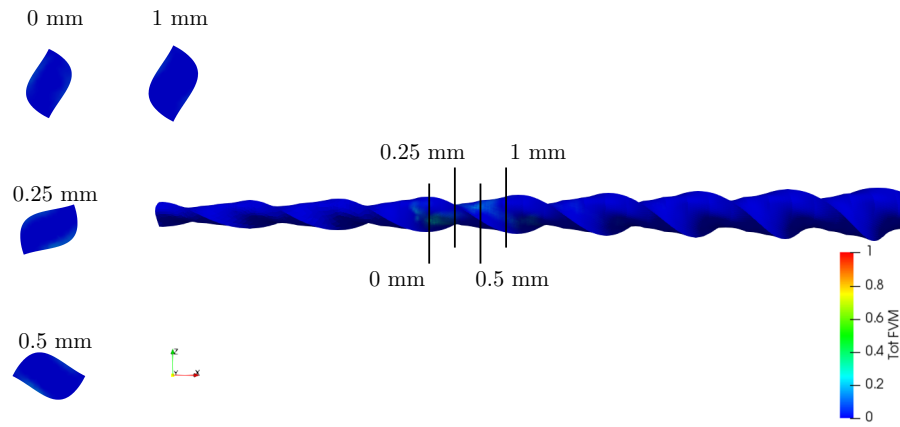


(c) Combined bending-torsion

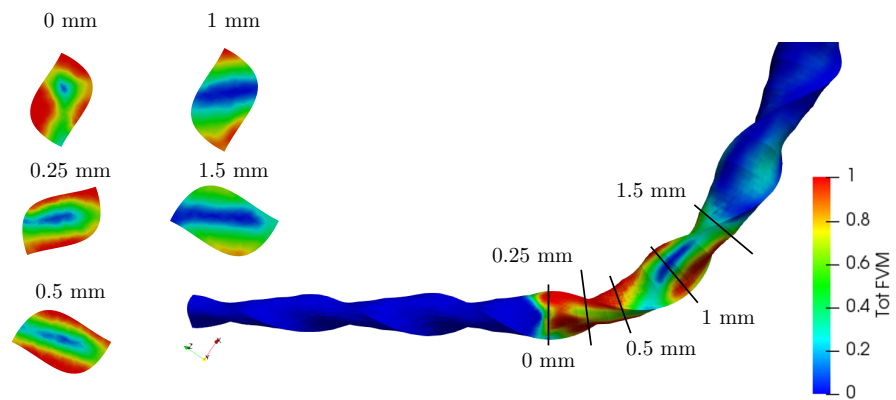
Figure 14: Stress distribution in an endodontic file prototype with a tip diameter of 0.28 mm, a taper of 4% and two edges cross section made of Cu-SC-SMA submitted to bending, torsion and combined bending-torsion loadings. Clamped area is 3 mm length.



(a) Bending



(b) Torsion



(c) Combines bending-torsion

Figure 15: Volume fraction of martensite distribution in an endodontic file prototype with a tip diameter of 0.28 mm, a taper of 4% and two edges cross section made of Cu-SC-SMA submitted to bending, torsion and combined bending-torsion loadings. Clamped area is 3 mm length.

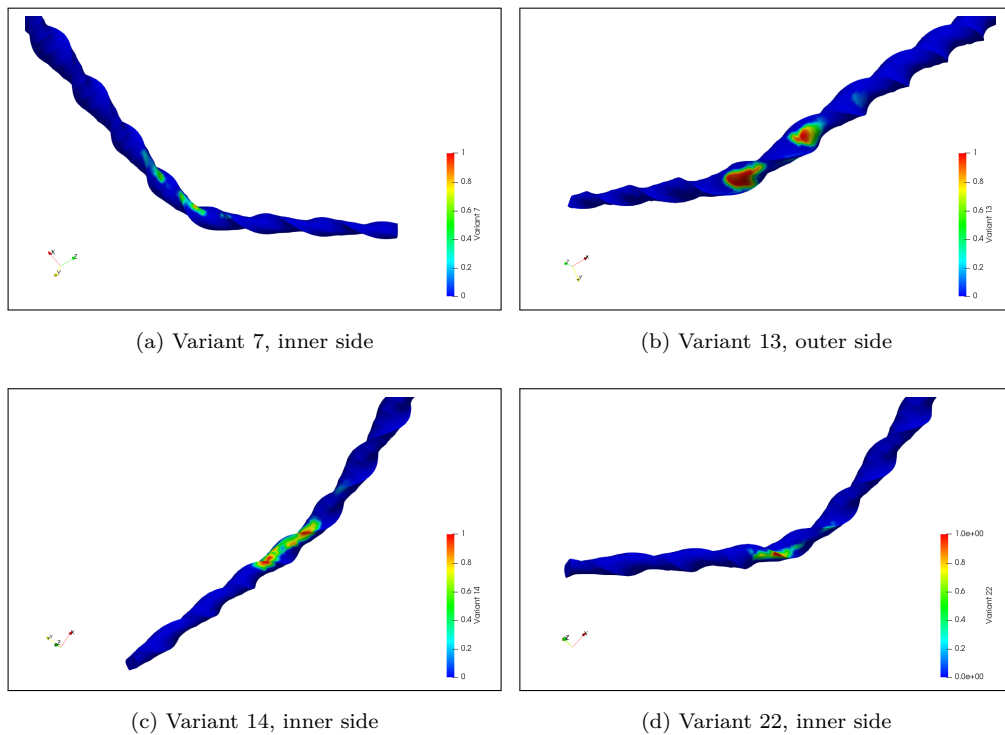

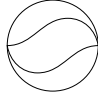
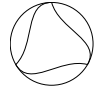


Figure 16: Distribution of variants 7, 13, 14 and 22 in combined bending-torsion loading. Their transformation direction and normal plane are given in table 1 and their interactions in table 2.

Table 5: Selected factors with their corresponding levels used in the Taguchi design of experiment.

Factor	Level 1	Level 2	Level 3
Cross Section	 0.5pt Asymmetric		
Tip diameter at 3 mm	0.40 mm	0.45 mm	0.50 mm
Taper	3 %	4 %	5 %
Pitch length	0.70 mm	0.85 mm	1.00 mm

449 and 14 are compatible but they occur for different loading levels in the bended
 450 area.

451 **4. Influence of the geometrical parameters on the response of the**
 452 **studied endodontic files**

453 After the identification of material parameters for the Cu-SC-SMA used
 454 to manufacture endodontic file prototypes, a Taguchi design of experiment is
 455 carried out numerically. It enables to analyse the influence of the geometrical
 456 parameters on the global response of these endodontic files during combined
 457 bending-torsion loading. It is designed to study multiple factors with a minimum
 458 number of simulations on the system and reduces the computation time.

459 *4.1. Selected factors and levels*

460 For this study, the selected factors are the cross section shape, the tip diam-
 461 eter at 3 mm from the tip, the taper and the pitch of the blade. Each factor
 462 has 3 levels represented in table 5.

Table 6: Taguchi orthogonal table with 4 factors at 3 levels.

Test	Factor 1 (Cross Section)	Factor 2 (Tip diameter at 3 mm)	Factor 3 (Taper)	Factor 4 (Pitch)
1	1	1	1	1
2	1	2	2	2
3	1	3	3	3
4	2	1	2	3
5	2	2	3	1
6	2	3	1	2
7	3	1	3	2
8	3	2	1	3
9	3	3	2	1

463 *4.2. Orthogonal table selection*

464 The selected set of factors and their levels are suitable for a Taguchi orthog-
465 onal table $L9(3^4)$ presented in table 6. Each factor is assigned to a column
466 where its values vary between the previously selected levels. Each line repre-
467 sents a numerical simulation to perform on the system with the levels of the
468 corresponding factor in columns. According to this table, it is possible to model
469 the corresponding blade geometries, which are presented in table 7.











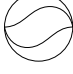







470 *4.3. Equivalent combined bending-torsion response*

471 The modeled endodontic file prototype responses are then numerically ana-
472 lyzed in combined bending-torsion. The adopted equivalent moment response
473 of combined bending-torsion M_{eq} is defined by the following relation:

$$M_{eq} = \sqrt{M_{bending}^2 + 3 \times M_{torsion}^2} \quad (11)$$

474 where $M_{bending}$ and $M_{torsion}$ are the moment responses of simulated prototypes
475 for bending and torsion respectively. Numerically obtained results are post-

Table 7: Selected factors with their corresponding level used in the Taguchi design of experiment according to table 6.

Prot.	Cross Section	$\varnothing_{at\ 3mm}$	Taper	Pitch	Modeled prototype
N#	[-]	[mm]	[%]	[mm]	
1		0.40	3	0.70	
2		0.45	4	0.85	
3		0.50	5	1.00	
4		0.40	4	1.00	
5		0.45	5	0.70	
6		0.50	3	0.85	
7		0.40	5	0.85	
8		0.45	3	1.00	
9		0.50	4	0.70	

476 treated to express the variation of the equivalent moment response around the
477 mean equivalent moment response of all tests.

478 *4.4. Numerical results issued from the Taguchi DOE*

479 Simulated responses of combined bending-torsion loadings for endodontic file
480 prototypes in Cu-SC-SMA are depicted in figure 17. Figure 18 is the graphical
481 representation of the mean response of the finite element model for a given factor
482 level. It consists in making the average of all the responses for the observed
483 factor level. Since the Taguchi table is orthogonal, the influence of other factor
484 levels is equivalent for each observed factor level.

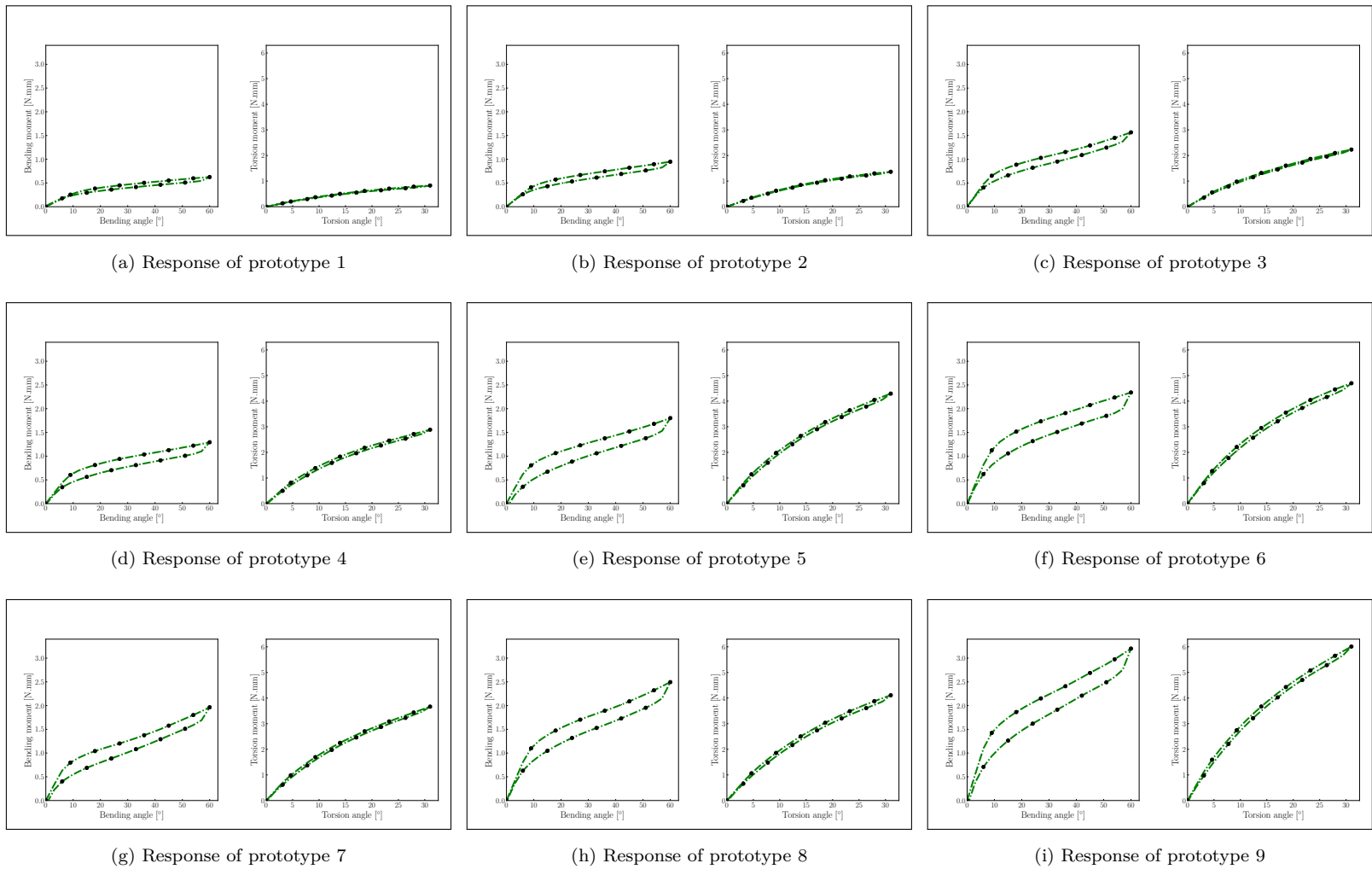


Figure 17: Responses in bending and torsion of the 9 finite element model prototypes.

485 According to the mean numerical responses of the factor levels, the best
486 parameters to reduce the global moment response in combined bending torsion
487 loading are: the asymmetric section shape, a diameter at 3 mm from the tip of
488 0.40 mm, a taper of 4% and a 1 mm pitch length. The evolution of the diameter
489 at 3 mm from the tip and the pitch length shows linear global response variation
490 while the taper seems to minimize this response for a value of 4%. The parameter
491 inducing the widest variation in the response is the cross section, followed by
492 the diameter at 3 mm from the tip , the taper and finally the pitch length.

493 .

494

495 5. Discussions

496 5.1. Introduction

497 In this section, experimental and numerical results are detailed and dis-
498 cussed. The first part presents experimental data of uniaxial tension, bending,
499 torsion and combined bending-torsion tests on Cu-SC-SMA wires and endodon-
500 tic file prototypes with their numerical comparison. The second part presents
501 the analysis of the results of the Taguchi DOE. The third part analyzes distri-
502 butions of stress and of martensitic variants in endodontic file prototypes loaded
503 in bending, torsion and combined bending-torsion.

504 5.2. *Experimental and numerical comparison of bending, torsion and combined* 505 *bending-torsion responses with Cu-SC-SMA endodontic file prototypes*

506 The comparison between the experimental and numerical responses in bend-
507 ing, torsion and combined bending-torsion loadings depicted in figures 11 for
508 wire and 13 for endodontic file prototype in Cu-SC-SMA, shows satisfactory
509 correlations. The material parameters, identified from DSC measurements, ten-
510 sion and torsion tests, allow to predict the Cu-SC-SMA response under tension
511 and torsion loadings as shown on figures 10 and 11b. Numerical prediction in
512 bending and combined bending-torsion tests on Cu-SC-SMA wires are slightly

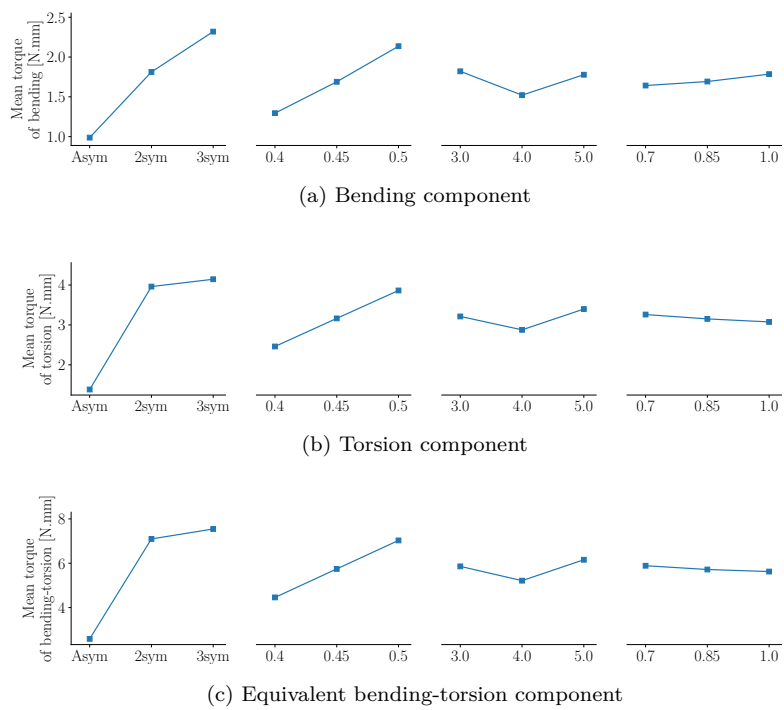


Figure 18: Mean responses according to level factor of endodontic file prototype in Cu-SC-SMA under combined bending-torsion.

513 less correlated with the experimental responses (figure 13). However, numerical
514 and experimental tendencies, such as the decrease of the transformation plateau
515 stiffness, observed between bending and combined bending-torsion is satisfacto-
516 rily predicted by the numerical model (figure 11a). In addition, elastic stiffness
517 increases and appearance of hysteresis in torsion component for numerical re-
518 sponse in combined bending-torsion loading (figure 11b) is well predicted by the
519 model. However, the numerical torsion response in combined bending-torsion
520 loading is under rated compared to experimental results.

521 The results issued from experimental and numerical predictions of the en-
522 dodontic instrument response under bending, torsion and combined bending-
523 torsion loadings are in satisfactory agreement. The differences between the two
524 results need to be solved with enhancement of the adopted finite element model.
525 On the one hand, elastic stiffness in torsion loading is underestimated (figure
526 13b). Likewise, in bending loading, the martensitic transformation predicted by
527 the numerical model shows a smaller hysteresis than the experimental response.

528 Several sources can explain these differences. On the experimental side, the
529 machining process with its imprecision may have an impact on the anticipated
530 shape of the prototypes. Likewise, the clamp of the tip, may generate addi-
531 tional stresses in the area close to the bended one. Moreover, high loading
532 amplitudes are severe to the prototype instrument, which is brought to its me-
533 chanical limits and over the clinically acceptable work condition. Furthermore,
534 these loading conditions may generate plasticity, which is not taken into ac-
535 count by the adopted thermomechanical constitutive model, and could explain
536 the difference in martensitic transformation between experimentally measured
537 and numerically predicted responses. The aforementioned causes also have an
538 impact on the modeling part. Indeed, the modeled prototype is assumed perfect,
539 without any machining imprecisions or microstrural change, like local recrystal-
540 lization. In addition, the model represents idealized clamping conditions of
541 contact between a plane and the tapered helicoidal triangular section shape.

542 On the other hand and despite all these difficulties, the micromechanical
543 model is able to closely reproduce the response of Cu-SC-SMA endontic file

544 prototypes under separated and combined bending-torsion loadings. The com-
545 parison of the bending component of the global numerical response between
546 bending and combined bending-torsion (figure 13a) shows that the model cor-
547 rectly predicts the decrease of the response after the start of martensitic tran-
548 sformation. For the torsion component, the decrease observed between combined
549 and separated torsion responses, on figure 13b, shows the model capacities to
550 reproduce global behavior of Cu-SC-SMA for complex loading cases.

551 *5.3. Distribution of stresses and volume fraction of martensite through the en-* 552 *doodontic file*

553 Figures 14 and 15 depict the stress and volume fraction of martensite in
554 endodontic file prototypes made of Cu-SC-SMA. It is visible that bending and
555 torsion loadings, in figures 14a and 14b respectively, generate high stress lev-
556 els, but only bending loading activates martensitic transformation (figure 15a).
557 Despite a high shear stress, concentrated in the middle of the blade faces of
558 the Cu-SC-SMA prototypes in torsion loading, a low quantity of martensite
559 is produced (figure 15b). Figure 14c shows how bending and torsion loadings
560 interact in combination and their influence on the martensitic transformation
561 level and its location (figure 15c). The Von Mises equivalent stress distribu-
562 tion for combined bending-torsion is a superposition of both normal and shear
563 stress distribution. The volume fraction of martensite is diffused according to
564 this stress distribution, except for stresses present in the middle of blade faces,
565 close to the 1 mm cut from the clamped area, and beyond (figure 15c). In the
566 case of combined bending-torsion loading, torsion increases the stiffness of the
567 instrument, leading to a more important martensitic transformation induced
568 by bending. Moreover, the complex geometry of the instrument leads to more
569 complex three-dimensional stress state. This directly influences the activation
570 process of martensitic variants (figure 11b and 13b). In addition, the flexibil-
571 ity gain in torsion of numerical responses between pure torsion and combined
572 bending-torsion loadings is visible with the transformation plateau on figure

573 **13b.** It is a global effect due to the martensitic transformation initiated by
574 bending.

575 Moreover, from the combined bending-torsion loading, the activated marten-
576 site variants are different for those activated for separated bending and torsion
577 loading. It induces a higher quantity of martensite and thus a higher transfor-
578 mation strain. Therefore, the induced global stiffness in torsion is lower for the
579 combined bending-torsion than in pure torsion. In addition, combining bending
580 and torsion leads to a higher failure level in torsion rotation than in the case of
581 pure torsion.

582 *5.4. Accurate geometry according to Taguchi DOE*

583 The Taguchi DOE allows to choose the best set of geometrical parameters,
584 for the response prediction of endodontic file prototypes in Cu-SC-SMA under
585 combined bending-torsion loading. This parameter set leads to the lowest stiff-
586 ness in combined bending-torsion. According to figure 18, it corresponds to an
587 asymmetric cross-section, with diameter at 3 mm from the tip of 0.4 mm, a
588 taper of 4% taper and 1 mm pitch length. The most influent parameter is the
589 cross-section. The asymmetrical part of the cross section offers the best op-
590 tion acting on the moment-rotation global responses. The taper has the lowest
591 influence on the moment-rotation global response. These results are obtained
592 with the numerical analysis and shown in figure 17. Moreover, during canal
593 root preparation, the diameter and the taper of the endodontic file are chosen
594 according to the size of the tooth canal. To go further, experimental investi-
595 gations should lead to a better prediction of the influence of each geometrical
596 parameter for endodontic files. Numerical simulations consider ideal geometry.
597 They should be replaced by the exact geometry of the manufactured endodontic
598 files with their imperfection.

599 **6. Conclusion and prospects**

600 This paper details the experimental and numerical response of a Cu-SC-SMA
601 endodontic file subjected to a bending-torsion loading. This new endodontic

602 instrument makes the preparation of root canal with higher simple or double
603 curvature easier. In addition it has very interesting antimicrobial properties. A
604 specific bending-torsion testing device is designed and manufactured in order
605 to carry out the experimental analysis. The corresponding obtained results
606 enable to identify the material parameters of a micromechanical constitutive
607 law, well adapted to Cu-SC-SMA. This law is coupled with a finite element
608 method to simulate the response of the studied endodontic file prototypes under
609 several loadings. It depicts an increase in the torsion strength of these Cu-SC-
610 SMA endodontic files when subjected to a combined bending-torsion loading
611 in comparison with a response for a pure torsion loading. The parameterized
612 geometrical model enables to analyze the influence of geometrical parameters
613 on the global response of these endodontic files. A Taguchi experimental plan is
614 applied for this analysis. It shows that the best parameter settings to decrease
615 moments in combined bending-torsion loading is an asymmetric section shape,
616 the lowest diameter at 3 mm from the tip of 0.4 mm, a taper of 4% and a pitch
617 length of 1 mm.

618 In conclusion, the obtained numerical and experimental results show that
619 the different responses of the instruments made of Cu-SC-SMA are close to
620 what was observed for commercial NiTi based instruments ([Schäfer and Tepel, 2001](#);
621 [Ninan and Berzins, 2013](#); [Santos et al., 2016](#)) and the sensitivity to geo-
622 metrical parameters is also globally the same. It should be possible to consider
623 endodontic files made of Cu-SC-SMA to maximize micro-organisms elimina-
624 tion while shaping the root canal, and to reduce the risks of failure during
625 endodontic treatment. The main challenges will be the optimization of their
626 shaping performances during the root canal preparation and the carrying out
627 of clinical tests in order to validate such performances in-vivo. Moreover, the
628 manufacturing process of the instrument could modify the Cu-SC-SMA behav-
629 ior. Additional features should be implemented in the micromechanical model
630 to fully exploit its potential to study microstructure of endodontic files under
631 rigorous constraints, such as plasticity or clamped conditions on the tip which
632 can be improved. Finally, future investigations should explore the shape mem-

633 ory effect of Cu-SC-SMA to investigate the possibilities of an increase of the
634 transformation capacities in torsion of this SMA, which can be favorable in the
635 endodontic domain.

636 **Acknowledgements**

637 The Cu-SC-SMA wires were supplied by the Nimesis Technology[®] company,
638 Mécleuves. The endodontic files were manufactured by the Coltene-Micromega[®]
639 company, Besançon. The DSC tests were carried out by the research team led
640 by Prof S. ARBAB-CHIRANI of the Laboratory IRDL, Brest, France. The
641 authors want to acknowledge their help for this study.

642 This work was undertaken in the framework of the Phd project of Paul XOLIN,
643 co-advised by Prof. Tarak BEN ZINEB and Prof. Marc ENGELS-DEUTSCH
644 and funded by the French agency ANRT "Association Nationale Recherche Tech-
645 nologie".

646 **References**

647 Ahamed, S.B.B., Vanajassun, P.P., Rajkumar, K., Mahalaxmi, S., 2018. Com-
648 parative Evaluation of Stress Distribution in Experimentally Designed Nickel-
649 titanium Rotary Files with Varying Cross Sections: A Finite Element Analy-
650 sis. *Journal of Endodontics* 44, 654–658. doi:<https://doi.org/10.1016/j.joen.2017.12.013>.

652 Aidasani, G.L., Mulay, S., Mehta, V.P., Anand, R., Mehta Vini, P., Anand, R.,
653 2017. Dentinal Defects in Endodontically Treated Teeth using NiTi Rotary
654 vs Reciprocating Endodontic Instruments- A Systematic Review. *Journal of*
655 *Clinical and Diagnostic Research* 11(12), ZE01–ZE04. doi:[10.7860/JCDR/2017/28764.10970](https://doi.org/10.7860/JCDR/2017/28764.10970).

657 Alcalde, M.P., Duarte, M.A.H., Bramante, C.M., de Vasconcelos, B.C.,
658 Tanomaru-Filho, M., Guerreiro-Tanomaru, J.M., Pinto, J.C., Só, M.V.R.,
659 Vivan, R.R., 2018. Cyclic fatigue and torsional strength of three different

660 thermally treated reciprocating nickel-titanium instruments. *Clinical Oral*
661 *Investigations* 22, 1865–1871. doi:[10.1007/s00784-017-2295-8](https://doi.org/10.1007/s00784-017-2295-8).

662 Arbab Chirani, R., Chevalier, V., Arbab Chirani, S., Calloch, S., 2011. Com-
663 parative analysis of torsional and bending behavior through finite-element
664 models of 5 NiTi endodontic instruments. *Oral Surgery, Oral Medicine, Oral*
665 *Pathology, Oral Radiology, and Endodontology* 111, 115–121. doi:<https://doi.org/10.1016/j.tripleo.2010.07.017>.

667 Belkahla, S., 1990. Elaboration et caractérisation de nouveaux alliages à mé-
668 moire de forme basse température type Cu-Al-Be. Ph.D. thesis. INSA, Lyon.

669 Bouvet, C., Calloch, S., Lexcelent, C., 2003. A phenomenological model for a
670 Cu-Al-Be shape memory alloy pseudoelasticity under complex loading. *Journal De Physique IV* 112, 201–204.

672 Casciati, F., Casciati, S., Faravelli, L., 2007. Fatigue characterization of a Cu-
673 based shape memory alloy. *Proceedings of the Estonian Academy of Sciences:*
674 *Physics, Mathematics* 56, 207–217.

675 Chemisky, Y., Duval, A., Patoor, E., Ben Zineb, T., 2011. Constitutive
676 model for shape memory alloys including phase transformation, martensitic
677 reorientation and twins accommodation. *Mechanics of Materials* 43, 361–
678 376. URL: <http://dx.doi.org/10.1016/j.mechmat.2011.04.003>, doi:[10.1016/j.mechmat.2011.04.003](https://doi.org/10.1016/j.mechmat.2011.04.003).

680 Chevalier, V., Pino, L., Arbab-Chirani, R., Calloch, S., Arbab-Chirani, S., 2018.
681 Experimental Validation of Numerical Simulations of a New-Generation NiTi
682 Endodontic File Under Bending. *Journal of Materials Engineering and Per-*
683 *formance* 27, 5856–5864. doi:[10.1007/s11665-018-3674-2](https://doi.org/10.1007/s11665-018-3674-2).

684 Chi, C.W., Li, C.C., Lin, C.P., Shin, C.S., 2017. Cyclic fatigue behavior of
685 nickel-titanium dental rotary files in clinical simulated root canals. *Journal*
686 *of the Formosan Medical Association* 116, 306–312. URL: <http://dx.doi.org/10.1016/j.jfma.2016.06.002>, doi:[10.1016/j.jfma.2016.06.002](https://doi.org/10.1016/j.jfma.2016.06.002).

- 688 Cissé, C., Zaki, W., Ben Zineb, T., 2016. A review of constitutive models and
689 modeling techniques for shape memory alloys. *International Journal of Plas-*
690 *ticity* 76, 244–284. URL: [http://dx.doi.org/10.1016/j.ijplas.2015.08.](http://dx.doi.org/10.1016/j.ijplas.2015.08.006)
691 [006](http://dx.doi.org/10.1016/j.ijplas.2015.08.006), doi:[10.1016/j.ijplas.2015.08.006](https://doi.org/10.1016/j.ijplas.2015.08.006).
- 692 Collard, C., Ben Zineb, T., 2012. Simulation of the effect of elastic precip-
693 itates in SMA materials based on a micromechanical model. *Composites*
694 *Part B: Engineering* 43, 2560–2576. URL: [http://dx.doi.org/10.1016/j.](http://dx.doi.org/10.1016/j.compositesb.2012.03.015)
695 [compositesb.2012.03.015](http://dx.doi.org/10.1016/j.compositesb.2012.03.015), doi:[10.1016/j.compositesb.2012.03.015](https://doi.org/10.1016/j.compositesb.2012.03.015).
- 696 De Arruda Santos, L., López, J.B., de Las Casas, E.B., De Azevedo Bahia, M.G.,
697 Buono, V.T.L., 2014. Mechanical behavior of three nickel-titanium rotary
698 files: A comparison of numerical simulation with bending and torsion tests.
699 *Materials Science and Engineering C* 37, 258–263. URL: [http://dx.doi.](http://dx.doi.org/10.1016/j.msec.2014.01.025)
700 [org/10.1016/j.msec.2014.01.025](http://dx.doi.org/10.1016/j.msec.2014.01.025), doi:[10.1016/j.msec.2014.01.025](https://doi.org/10.1016/j.msec.2014.01.025).
- 701 Entemeyer, D., Patoor, E., Eberhardt, A., Berveiller, M., 2000. Strain rate
702 sensitivity in superelasticity. *International Journal of Plasticity* 16, 1269–
703 1288. doi:[https://doi.org/10.1016/S0749-6419\(00\)00010-3](https://doi.org/10.1016/S0749-6419(00)00010-3).
- 704 Ferreira, F., Adeodato, C., Aboud, I.B.L., Scelza, P., Scelza, M.Z., 2017. Move-
705 ment kinematics and cyclic fatigue of NiTi rotary instruments: A systematic
706 review. *International Endodontic Journal* 50, 143–152.
- 707 Gavini, G., dos Santos, M., Caldeira, C.L., Machado, M.E.d.L., Freire, L.G.,
708 Iglecias, E.F., Peters, O.A., Candeiro, G.T.d.M., 2018. Nickel-titanium in-
709 struments in endodontics: A concise review of the state of the art. *Brazilian*
710 *Oral Research* 32, 44–65. doi:[10.1590/1807-3107bor-2018.vol132.0067](https://doi.org/10.1590/1807-3107bor-2018.vol132.0067).
- 711 Grass, G., Rensing, C., Solioz, M., 2011. Metallic copper as an antimicrobial
712 surface. *Applied and Environmental Microbiology* 77, 1541–1547. doi:[10.](https://doi.org/10.1128/AEM.02766-10)
713 [1128/AEM.02766-10](https://doi.org/10.1128/AEM.02766-10).
- 714 Ha, J.H., Kwak, S.W., Sigurdsson, A., Chang, S.W., Kim, S.K., Kim, H.C.,
715 2017. Stress Generation during Pecking Motion of Rotary Nickel-titanium

- 716 Instruments with Different Pecking Depth. *Journal of Endodontics* 43, 1688–
717 1691. doi:[10.1016/j.joen.2017.04.013](https://doi.org/10.1016/j.joen.2017.04.013).
- 718 Hartemann, P., Goepfert, M., Blech, M.F., 1995. Bactericidal effect of hydrogen
719 peroxide on *Escherichia coli*. *Ann. Med. de l'Est NANCY* 34, 85–88.
- 720 Int. Org. for Standardization, 2008. Root-canal instrument - Part1: General
721 requirements and test methods. volume ISO 3630-1.
- 722 Jamleh, A., Alghaihab, A., Alfadley, A., Alfawaz, H., Alqedairi, A., Alfouzan,
723 K., 2019. Cyclic Fatigue and Torsional Failure of EdgeTaper Platinum
724 Endodontic Files at Simulated Body Temperature. *Journal of Endodon-*
725 *tics* 45, 611–614. URL: <https://doi.org/10.1016/j.joen.2019.02.008>,
726 doi:[10.1016/j.joen.2019.02.008](https://doi.org/10.1016/j.joen.2019.02.008).
- 727 Kaouache, B., Berveiller, S., Inal, K., Eberhardt, A., Patoor, E., 2004. Stress
728 analysis of martensitic transformation in Cu-Al-Be polycrystalline and single-
729 crystalline shape memory alloy. *Materials Science and Engineering A* 378,
730 232–237. doi:[10.1016/j.msea.2003.10.348](https://doi.org/10.1016/j.msea.2003.10.348).
- 731 Karatas, E., Arslan, H., Bükler, M., Seçkin, F., Çapar, I.D., 2016. Effect of
732 movement kinematics on the cyclic fatigue resistance of nickel–titanium in-
733 struments. *International Endodontic Journal* 49, 361–364. doi:[10.1111/iej.](https://doi.org/10.1111/iej.12453)
734 [12453](https://doi.org/10.1111/iej.12453).
- 735 Kim, H.C., Kwak, S.W., Cheung, G.S.P., Ko, D.H., Chung, S.M., Lee, W., 2012.
736 Cyclic Fatigue and Torsional Resistance of Two New Nickel-Titanium Instru-
737 ments Used in Reciprocation Motion: Reciproc Versus WaveOne. *Journal of*
738 *Endodontics* 38, 541–544. doi:[https://doi.org/10.1016/j.joen.2011.11.](https://doi.org/10.1016/j.joen.2011.11.014)
739 [014](https://doi.org/10.1016/j.joen.2011.11.014).
- 740 Martins, R.F., Fernandes, A., Loios, G., Ginjeira, A.A., 2017. Fatigue resistance
741 of rotary endodontic files subjected to planar and non-planar curvatures in-
742 duced by in vitro tooth canals. *International Journal of Structural Integrity*
743 8, 656–669. doi:[10.1108/IJSI-01-2017-0005](https://doi.org/10.1108/IJSI-01-2017-0005).

- 744 McGuigan, M.B., Louca, C., Duncan, H.F., 2013. Endodontic instrument
745 fracture: causes and prevention. *British Dental Journal* 214, 341–348.
746 doi:[10.1038/sj.bdj.2013.324](https://doi.org/10.1038/sj.bdj.2013.324).
- 747 Merzouki, T., Collard, C., Bourgeois, N., Ben Zineb, T., Meraghni, F., 2010.
748 Coupling between measured kinematic fields and multicrystal SMA finite ele-
749 ment calculations. *Mechanics of Materials* 42, 72–95. URL: [http://dx.doi.](http://dx.doi.org/10.1016/j.mechmat.2009.09.003)
750 [org/10.1016/j.mechmat.2009.09.003](http://dx.doi.org/10.1016/j.mechmat.2009.09.003), doi:[10.1016/j.mechmat.2009.09.](https://doi.org/10.1016/j.mechmat.2009.09.003)
751 [003](https://doi.org/10.1016/j.mechmat.2009.09.003).
- 752 Niclaeys, C., Ben Zineb, T., Arbab Chirani, S., Patoor, E., 2002. Determination
753 of the interaction energy in the martensitic state. *International Journal of*
754 *plasticity* 18, 1619–1647.
- 755 Ninan, E., Berzins, D.W., 2013. Torsion and bending properties of shape mem-
756 ory and superelastic nickel-titanium rotary instruments. *Journal of Endodon-*
757 *tics* 39, 101–104. URL: <http://dx.doi.org/10.1016/j.joen.2012.08.010>,
758 doi:[10.1016/j.joen.2012.08.010](https://doi.org/10.1016/j.joen.2012.08.010).
- 759 Ojeil, M., Jermann, C., Holah, J., Denyer, S.P., Maillard, J.Y., 2013. Evalu-
760 ation of new invitro efficacy test for antimicrobial surface activity reflecting
761 UK hospital conditions. *Journal of Hospital Infection* 85, 274–281. URL:
762 <http://dx.doi.org/10.1016/j.jhin.2013.08.007>, doi:[10.1016/j.jhin.](https://doi.org/10.1016/j.jhin.2013.08.007)
763 [2013.08.007](https://doi.org/10.1016/j.jhin.2013.08.007).
- 764 Padavala, S., Ganapathy, D., 2019. Fatigue in rotary endodontic instruments -
765 A review. *Drug Invention Today* 11, 671–676.
- 766 Patoor, E., Eberhardt, A., Berveiller, M., 1996. Micromechanical Modelling of
767 Superelasticity in Shape Memory Alloys. *Le Journal de Physique IV* 06, C1–
768 277–C1–292. URL: <http://www.edpsciences.org/10.1051/jp4:1996127>,
769 doi:[10.1051/jp4:1996127](https://doi.org/10.1051/jp4:1996127).
- 770 Pedrinha, V.F., da Silva Brandao, J.M., Pessoa, O.F., Rodrigues, P.d.A., 2018.
771 Influence of File Motion on Shaping, Apical Debris Extrusion and Dentinal

- 772 Defects: A Critical Review. *Open Dentistry Journal* 12, 189–201. doi:[10.2174/1874210601812010189](https://doi.org/10.2174/1874210601812010189).
773
- 774 Peultier, B., Ben Zineb, T., Patoor, E., 2006. Macroscopic constitutive law of
775 shape memory alloy thermomechanical behaviour. Application to structure
776 computation by FEM. *Mechanics of Materials* 38, 510–524. doi:[10.1016/j.mechmat.2005.05.026](https://doi.org/10.1016/j.mechmat.2005.05.026).
777
- 778 Prado, J.V., Vidal, A.R., Durán, T.C., 2012. Application of copper bactericidal
779 properties in medical practice. *Revista Medica de Chile* 140, 1325–1332.
780 doi:[10.4067/S0034-98872012001000014](https://doi.org/10.4067/S0034-98872012001000014).
- 781 Prados-Privado, M.M.M., Rojo, R., Ivorra, C., Prados-Frutos, J.C., Carlos
782 Prados-Frutos, J., Prados-Frutos, J.C., 2019. Finite element analysis comparing
783 WaveOne, WaveOne Gold, Reciproc and Reciproc Blue responses with
784 bending and torsion tests. *Journal of the Mechanical Behavior of Biomedical
785 Materials* 90, 165–172. URL: <https://doi.org/10.1016/j.jmbbm.2018.10.016>, doi:[10.1016/j.jmbbm.2018.10.016](https://doi.org/10.1016/j.jmbbm.2018.10.016).
786
- 787 Rios-Jara, D., Planes, A., Manosa, L.I., Ortin, J., Belkahla, S., Morin, M.,
788 Guénin, G., Macqueron, J.L., 1991. Martensitic transition entropy change
789 and elastic constants of Cu-Al-Be alloys. *Le Journal de Physique IV* 01,
790 C4–283–C5–288. doi:[10.1051/jp4:1991443](https://doi.org/10.1051/jp4:1991443).
- 791 Rodrigues, C.T., Duarte, M.A.H., de Almeida, M.M., de Andrade, F.B., Bernardini,
792 N., 2016. Efficacy of CM-Wire, M-Wire, and Nickel-Titanium Instruments for
793 Removing Filling Material from Curved Root Canals: A Micro-Computed Tomography
794 Study. *Journal of Endodontics* 42, 1651–1655. URL: <http://dx.doi.org/10.1016/j.joen.2016.08.012>, doi:[10.1016/j.joen.2016.08.012](https://doi.org/10.1016/j.joen.2016.08.012).
795
796
- 797 Santos, L.D.A., Resende, P.D., Bahia, M.G.D.A., Buono, V.T.L., 2016. Effects of R-Phase on
798 Mechanical Responses of a Nickel-Titanium Endodontic Instrument: Structural
799 Characterization and Finite Element Analysis. *Scientific World Journal* , 11doi:[10.1155/2016/7617493](https://doi.org/10.1155/2016/7617493).
800

- 801 Schaefer, E., Oitzinger, M., 2008. Cutting Efficiency of Five Different Types
802 of Rotary Nickel-Titanium Instruments. *Journal of Endodontics* 34, 198–200.
803 doi:<https://doi.org/10.1016/j.joen.2007.10.009>.
- 804 Schäfer, E., Tepel, J., 1999. Relationship between design features of endodontic
805 instruments and their properties. Part 2. Instrumentation of curved canals.
806 *Journal of Endodontics* 25, 56–59. doi:[10.1016/S0099-2399\(99\)80401-4](https://doi.org/10.1016/S0099-2399(99)80401-4).
- 807 Schäfer, E., Tepel, J., 2001. Relationship Between Design Features of Endodon-
808 tic Instruments and Their Properties . Part 3 . Resistance to Bending and
809 Fracture. *Journal of Endodontics* 27, 299–303.
- 810 Shen, Y., Qian, W., Abtin, H., Gao, Y., Haapasalo, M., 2011. Fatigue testing
811 of controlled memory wire nickel-titanium rotary instruments. *Journal of En-*
812 *dodontics* 37, 997–1001. URL: [http://dx.doi.org/10.1016/j.joen.2011.](http://dx.doi.org/10.1016/j.joen.2011.03.023)
813 [03.023](https://doi.org/10.1016/j.joen.2011.03.023), doi:[10.1016/j.joen.2011.03.023](https://doi.org/10.1016/j.joen.2011.03.023).
- 814 Siredey, N., Patoor, E., Berveiller, M., Eberhardt, A., 1999. Constitutive equa-
815 tions for polycrystalline thermoelastic shape memory alloys.: Part I. Intra-
816 granular interactions and behavior of the grain. *International Journal of Solids*
817 *and Structures* 36, 4289–4315. URL: [http://www.sciencedirect.com/](http://www.sciencedirect.com/science/article/pii/S0020768398001966)
818 [science/article/pii/S0020768398001966](https://doi.org/10.1016/S0020-7683(98)00196-6), doi:[10.1016/S0020-7683\(98\)](https://doi.org/10.1016/S0020-7683(98)00196-6)
819 [00196-6](https://doi.org/10.1016/S0020-7683(98)00196-6).
- 820 Sittner, P., Hashimoto, K., Kato, M., Tokuda, M., 2003. Stress induced marten-
821 sitic transformations in tension/torsion of CuAlNi single crystal tube. *Scripta*
822 *Materialia* 48, 1153–1159. doi:[10.1016/S1359-6462\(02\)00583-3](https://doi.org/10.1016/S1359-6462(02)00583-3).
- 823 Spratt, D.A., Pratten, J., Wilson, M., Gulabivala, K., 2001. An in vitro evalua-
824 tion of the antimicrobial efficacy of irrigants on biofilms of root canal isolates.
825 *International Endodontic Journal* 34, 300–307.
- 826 Tokuda, M., Sittner, P., Takakura, M., Men, Y., 1995. Experimetnal stuy
827 on performances in Cu-based shape memory alloy under multi-axial loading

- 828 contions. *Materials Science Research International* 1, 260—265. doi:[10.1017/CB09781107415324.004](https://doi.org/10.1017/CB09781107415324.004), [arXiv:arXiv:1011.1669v3](https://arxiv.org/abs/1011.1669v3).
829
- 830 Vincent, M., Duval, R.E., Hartemann, P., Engels-Deutsch, M., 2018. Contact
831 killing and antimicrobial properties of copper. *Journal of Applied Microbiol-*
832 *ogy* 124, 1032–1046. doi:[10.1111/jam.13681](https://doi.org/10.1111/jam.13681).
- 833 Vincent, M., Thiébaud, F., Bel Haj Khalifa, S., Engels-Deutsch, M., Ben Zineb,
834 T., 2015. Finite Element Analysis of a Copper Single Crystal Shape Memory
835 Alloy-Based Endodontic Instruments. *Journal of Materials Engineering and*
836 *Performance* 24, 4128–4139. doi:[10.1007/s11665-015-1677-9](https://doi.org/10.1007/s11665-015-1677-9).
- 837 Vincent, M., Xolin, P., Gevrey, A.M., Thiebaud, F., Engels-Deutsch, M., Ben
838 Zineb, T., 2017. Experimental and numerical analysis of penetration/removal
839 response of endodontic instrument made of single crystal Cu-based SMA:
840 comparison with NiTi SMA instruments. *Smart Materials and Structures* 26,
841 0–35. doi:[10.1088/1361-665X/aa5f0b](https://doi.org/10.1088/1361-665X/aa5f0b).
- 842 Xolin, P., Becker, S., Thiébaud, F., Engels-Deutsch, M., Ben Zineb, T., 2020.
843 Combined bending–torsion testing device for characterization of shape mem-
844 ory alloy endodontic files. *Journal of Intelligent Material Systems and Struc-*
845 *tures* 31, 1763–1781. doi:<https://doi.org/10.1177/1045389X20932218>.
- 846 Zelada, G., Varela, P., Martín, B., Bahillo, J.G., Magán, F., Ahn, S., 2002. The
847 effect of rotational speed and the curvature of root canals on the breakage of
848 rotary endodontic instruments. *Journal of Endodontics* 28, 540–542. doi:[10.1097/00004770-200207000-00014](https://doi.org/10.1097/00004770-200207000-00014).
849
- 850 Zinelis, S., Darabara, M., Takase, T., Ogane, K., Papadimitriou, G.D., 2007.
851 The effect of thermal treatment on the resistance of nickel-titanium rotary files
852 in cyclic fatigue. *Oral Surgery Oral Medicine Oral Pathology Oral Radiology*
853 *and Endodontology* 103, 843–847. doi:[10.1016/j.tripleo.2006.12.026](https://doi.org/10.1016/j.tripleo.2006.12.026).